Nano Today 27 (2019) 48–72

Contents lists available at ScienceDirect

Nano Today

journal homepage: www.elsevier.com/locate/nanotoday

Review

Gold nanorods-based hybrids with tailored structures for photoredox catalysis: fundamental science, materials design and applications

Chuang Han[a,b], Ming-Yu Qi[a,b], Zi-Rong Tang[a,b], Jinlong Gong[c], Yi-Jun Xu[a,b,*]

[a] State Key Laboratory of Photocatalysis on Energy and Environment, College of Chemistry, Fuzhou University, Fuzhou, 350116, PR China
[b] College of Chemistry, New Campus, Fuzhou University, Fuzhou, 350108, PR China
[c] School of Chemical Engineering and Technology, Tianjin University, Collaborative Innovation Center of Chemical Science and Engineering (Tianjin), Tianjin, 300072, PR China

ARTICLE INFO

Article history:
Received 14 January 2019
Received in revised form 18 March 2019
Accepted 1 May 2019
Available online 23 May 2019

Keywords:
Gold nanorods
Surface plasmon resonance
Redox catalysis
Hybrid structure
Solar energy conversion

ABSTRACT

Gold nanorods (Au NRs) have received extensive attention owing to their extremely attractive applications in photoredox catalysis, plasmon-enhanced spectroscopy, biomedical technologies and optoelectronic devices. Enabled by the unique and tunable surface plasmon resonance (SPR), anisotropic Au NRs can interact with and harvest incident light covering the much of the solar spectrum. As such, they may serve as unusual media to supply energetic hot charge carriers, generate heat, and provide strong local electric field and reactive site for redox reactions through different mechanisms. In this review, we present a comprehensive overview on the burgeoning field of Au NRs-based materials for solar energy conversion. We firstly provide a detailed elucidation of the key underpinning science for plasmonic Au NRs and Au NRs-mediated catalysis. The possible charge transfer processes and corresponding roles of Au NRs played in different photoredox catalysis systems are demonstrated, followed by introducing the latest advances in constructing Au NRs-based hybrids with tailored structure. The applications of the hybrids in photoinduced catalysis, photothermal catalysis and photoelectrochemical catalysis are then discussed. Particularly, the process-intensified engineering strategies to maximize solar energy conversion efficiency are further highlighted based on some typical examples. Finally, the perspectives on future research trends and challenges in rational design and deliberate construction of Au NRs-mediated photoredox catalysis systems in a smart configuration are proposed.

Contents

Abbreviations: NR, nanorod; NIR, near infrared; SPR, surface plasmon resonance; UV, ultraviolet; CB, conduction band; PL, photoluminescence; Vis, visible; 0D, zero-dimensional; 3D, three-dimensional; NP, nanoparticle; 1D, one-dimensional; SEM, scanning electron microscopy; VB, valence band; 2D, two-dimensional; XRD, X-ray diffraction; NWs, nanowires; QDs, quantum dots; PSS, poly-styrene sulfonate; HD, hot-dog; NRAs, nanorod arrays; LEF, local electric field; NSP, nanosteps; BP, black phosphorus; SDS, sodium dodecyl sulfate; NS, nanosheet; RhB, Rhodamine B; PIC, photoinduced redox catalysis; GR, graphene; NB, nitrobenzene; PTC, photothermal catalysis; MOF, metal-organic-framework material; PEC, photoelectrochemical catalysis; TEM, transmission electron microscopy; BA, benzyl alcohol; PRET, plasmon-induced resonant energy transfer; BAD, benzaldehyde; HET, hot electron generation and transfer; CTAB, cetyltrimethylammonium bromide; HER, hydrogen evolution reaction; MPA, mercaptopropionic acid; AQE, apparent quantum efficiency; OEC, oxygen evolution co-catalyst; LUMO, lowest unoccupied molecular orbital; ROS, reactive oxygen species; IPCE, incident photon-to-electron conversion efficiency; FDTD, finite difference time domain; ABDA, 9,10-anthracenediyl-bis(methylene) dimalonic acid.

* Corresponding author at: College of Chemistry, New Campus, Fuzhou University, Fuzhou, 350108, PR China.
E-mail address: yjxu@fzu.edu.cn (Y.-J. Xu).

https://doi.org/10.1016/j.nantod.2019.05.001
1748-0132/

Introduction

Solar energy is a major source of renewable energy with the potential to meet the energy demand and support the sustainable development of the world [1–7]. Since fossil fuels have been excessively consumed, there is a natural trend to explore alternative approaches to serve human activities through sunlight harvesting and its conversion into usable forms [7,8]. In general, solar energy can be harnessed and converted into various kinds of energy, including chemical and thermal energy, and electricity, through photochemical, photothermal and photovoltaic processes, respectively [4,7,9–11]. Photoredox catalysis, where photons are absorbed by catalysts to generate the charge carriers that can participate in photochemical reactions under suitable conditions, remains as one of the leading hubs of research for solar energy conversion [12–14]. Recent developments suggest that the metal-based plasmonic composites are the promising and cutting-edge research materials for photoredox catalysis [15–18].

Among the various types of metallic nanostructures [19–21], the utilization of Au NRs has attracted particular attention for the development of solar energy conversion arising from the intriguing light-harvesting, highly focused electric field, effective photothermal conversion and unique hot electron generation properties of Au NRs [22]. Compared with the widely used spherical Au or Ag nanoparticles (NPs) that possess only one narrow SPR absorption band in short-wavelength visible (Vis) or ultraviolet (UV) window, Au NRs exhibit two distinct plasmon resonances termed as transverse SPR (T-SPR) and longitudinal SPR (L-SPR) resulting from their anisotropic morphology [23]. The T-SPR of Au NRs is mainly located at 520–540 nm, matching excellently with the peak wavelength of solar spectrum, while the L-SPR can be tuned from visible to near infrared (NIR) light range by tailoring the aspect ratio and the overall size of nanorod (NR) [24], thus paving the way for solar energy conversion by harnessing the Vis-NIR light.

Nowadays, uniform Au NRs with tunable SPR absorption have been well produced by diverse wet chemical synthesis routes [25–27]. Furthermore, Au NRs can be assembled into a number of superstructures and coupled with other functional components in different geometries owing to their anisotropic one-dimensional (1D) nature [28,29]. These allow the plasmonic properties of Au NRs to be easily tuned to cultivate the specific applications. Hitherto, there have been some excellent reviews focusing on the synthesis, physicochemical properties, functionalization, and biomedical/sensing applications of Au NRs [23,24,30,31]. But the flourishing field of diverse Au NRs-based hybrids with tailored structures for solar energy conversion has not been systematically elaborated with the pace of progress in this research area. In view of the fact that the optical, electronic and catalytic properties of Au NRs-based nanostructures can be synthetically modulated, the Au NRs offer an exciting platform to explore the structure-plasmon-catalysis interplays of plasmonic catalysts, and understand the intricate effects related to surface plasmons on the targeted photoredox reactions.

Herein, we provide an up-to-date review on various Au NRs-based hybrids with tailored structures, focusing on their properties and recent application progress in photoinduced catalysis, photoelectrochemical catalysis and photothermal catalysis (Fig. 1). To enable a better understanding of the physical and chemical processes underlying these photoredox catalysis applications, some basic but essential properties of Au NRs and the concepts and fundamentals about SPR-mediated catalysis are briefly introduced. Following this, the possible charge transfer processes and the multifarious roles of Au NRs played in the Au NRs-mediated catalysis are discussed, which would exemplify the unique structure-property relationships of Au NRs-based nanostructures. After addressing the synthetic chemistry and structural characteristics of four typical Au NRs-based hybrids, particular attention is then paid to the recent application developments and the process-intensified engineering strategies that maximize the performance of hybrid materials in various photoredox catalysis processes. Finally, we end with casting a perspective on the challenges and opportunities for future development of Au NRs-based nanostructures in solar energy conversion. It is hoped that the basic knowledge, very recent developments, critical insights and performance optimization strategies elucidated in this review could help to shed light on understanding fundamental photophysics of Au NRs-mediated photoredox catalysis, offer useful guidelines to design high performance Au NRs-based catalysts and other plasmonic devices, and give further inspirations to push this research area into the next stage.

Fundamentals of Au NRs-mediated photoredox catalysis

Properties of Au NRs

The phenomenon of symmetry breaking is pervasive throughout science and nature [32]. For the growth of metal crystals, symmetry breaking is the crucial step to generate a novel nanoparticle morphology or structure that exhibits new properties [33]. The structure-property relationships of such nanoparticle are perhaps well exemplified by Au NRs. Fig. 2a shows different structural models of the Au NRs, with their specific planes. Compared with spherical Au NPs, which consist of only (111) and (100) surface facets [34], the surface of the Au NRs is composed of side-facets (110) or (100) and edge-facets (111) or (100) [29,35]. The coexistence of these facets induces the anisotropic shapes of the Au NRs and results in their unique optical, electric and catalytic properties [36]. In discussions of SPR-mediated catalysis associated with Au

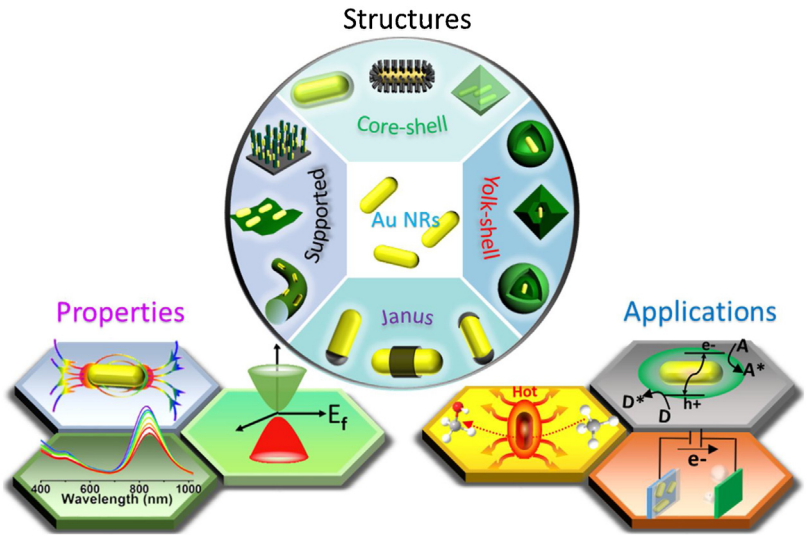

Fig. 1. Schematic diagram of the contents of the present review.

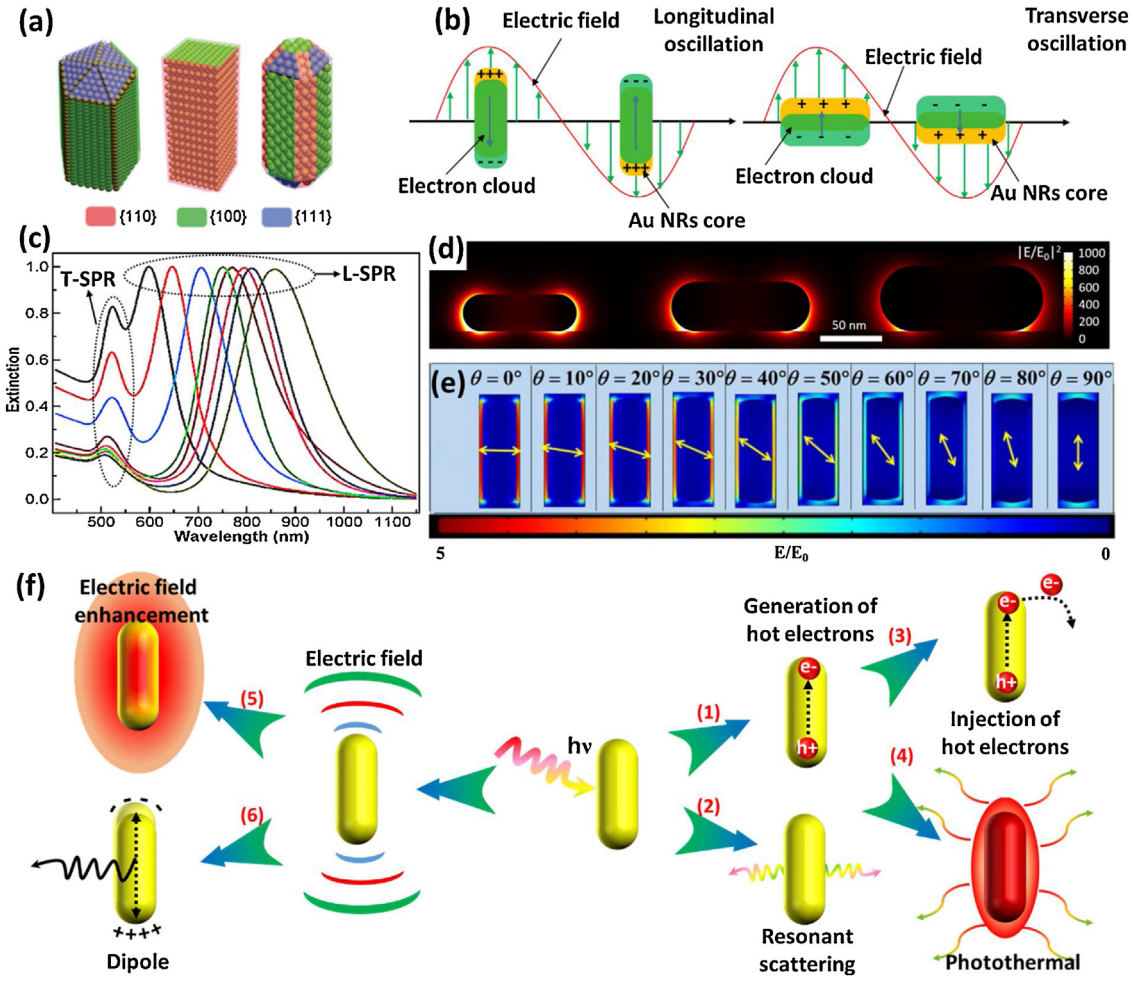

Fig. 2. (a) Structural models of Au NRs with different surface facet configurations. (b) Schematic illustration of L-SPR and T-SPR excitation for Au NRs. (c) L-SPR and T-SPR absorption bands of Au NRs with different aspect ratio. (d) Theoretical simulated LEF of Au NRs with different sizes. (e) Polarization dependence of the LEF intensity distribution obtained from the numerical calculation on one Au NR excited at the wavelength of 500 nm. The polarization angles (θ) are relative to the short axis of NR. (f) A scenario for the processes resulting from SPR. (a) Reproduced with permission from [29]. Copyright 2011, Royal Society of Chemistry. (c) Reproduced with permission from [38]. Copyright 2014, Wiley. (d) Reproduced with permission from [45]. Copyright 2016, American Chemical Society. (e) Reproduced with permission from [44]. Copyright 2017, The Optical Society.

NRs, two crucial issues that determine the solar energy conversion efficiency have to be taken into account: light harvesting ability, and electric field distribution, both of which are strongly correlated with the structure of Au NRs.

Au NRs with cylindrical symmetry usually exhibit two SPR modes (Fig. 2b): the L-SPR mode related to the electron oscillation along the length direction and the T-SPR mode arising from the transverse electron oscillation. When Au NRs are irradiated with incident light, the electric field of the light interacts with the free electrons in the Au NRs, leading to a charge separation between the free electrons and the ionic Au core. The Coulomb repulsion among the free electrons acting as a restoring force pushes the free electrons to move in the opposite direction, which results in the collective oscillation of electrons or, in another words, the excitation of SPR [24,37]. The occurrence of SPR also results in a strong absorption of incident light (Fig. 2c). The T-SPR absorption is found to be insensitive to the changes in the size of Au NRs, whereas the L-SPR shows a red-shift with the increase of aspect ratio (R) of Au NRs and is very sensitive to any change of the refractive index (or dielectric functions) [38]. In aqueous solution, the L-SPR absorption maximum (λ_{max}) is linearly proportional to the aspect ratio as the following relationship [24,39,40]:

$$\lambda_{max} = 95R + 420 \quad (1)$$

This indicates the possibility of optical tuning of Au NRs by simply varying their aspect ratio, which is different from spheres where the SPR only slightly red-shifts with increasing particle size [41,42]. Besides the geometry effects, the electron density and surrounding refractive index are also the important factors that affect the plasmon resonance of Au NRs. From Gans theory, one can derive the L-SPR wavelength ($\lambda_{L\text{-}SPR}$) of an Au NR by the following equations [23,43]:

$$\lambda_{L-SPR} = \lambda_p \sqrt{\varepsilon_\infty + \left(\frac{1}{L} - 1\right)\varepsilon_m} \quad (2)$$

$$\lambda_p = \sqrt{\frac{2\pi^2 c^2 m \varepsilon_\infty}{Ne^2}} \quad (3)$$

Where ε_∞ is the high-frequency dielectric constant of Au NRs, L is the depolarization factor along the length axis of the Au NRs, ε_m is the dielectric functions of the surrounding medium, c is the speed of light, m is the electron effective mass in Au NRs, e is the elemental charge, and N is the conduction electron density. The expressions above clearly show that increasing the number of free electrons or decreasing the dielectric functions will result in a blue-shift of the L-SPR wavelength of Au NRs.

Another prominent property of Au NRs is the SPR-mediated local electric field (LEF) enhancement. Upon resonant excitation, SPR can break the diffraction limit and concentrate light into a nanoscale region. The strong light localization makes the optical electric field near the surface of Au NRs largely enhanced [44]. Fig. 2d shows the field intensity enhancement distribution contours of Au NRs with different sizes obtained from finite-element method simulations [45]. The field intensity enhancement relative to the far-field excitation light intensity are maximal at the Au NRs surface and decay approximately exponentially away from the surface [46,47], which can be tailored by controlling the aspect ratio and curvature of Au NRs [48]. In general, the sharper the Au NRs are, the stronger the field enhancement is. The intensity and distribution of field enhancement are also dependent on the external conditions, such as the wavelength and polarization angle of excitation light [33]. When the wavelength of the excitation light is close to the SPR absorption bands of Au NRs nanocrystals, the field intensity enhancement factors will be enhanced [49]. As shown in Fig. 2e, the maximum field enhancement regions rotate away from the Au NRs side synchronously as the excitation polarization varies gradually from the transverse to longitudinal directions [44]. This rotation is ascribed to the phase difference between the longitudinal and transverse electron oscillations under the resonance excitation [50].

Mechanisms of Au NRs-mediated photoredox catalysis

The resonant excitation of Au NRs gives rise to a collection of optical and electronic effects and induces intense LEF enhancement near the surface of Au NRs [51,52]. A scenario for the processes resulting from SPR excitation is briefly illustrated in Fig. 2f. The surface plasmons in excited state can decay (1) non-radiatively by transferring the energy to the energetic charge carriers (i.e., hot electrons and holes), or (2) radiatively by scattering of resonant photons [15]. The energetic charge carriers can (3) transfer to the surroundings (e.g., semiconductors) or (4) relax by locally heating the nanostructure [53]. On the other hand, the intense LEF near the surface of Au NRs can interact with semiconductors or molecules through (5) near-field or (6) dipole-dipole coupling [54,55]. Among these process, three important effects related to surface plasmons may impact the redox reactions: generation and injection of hot electrons (process 1 and 3, respectively), photothermal conversion (process 4), and LEF enhancement (process 5).

Hot electron generation and transfer (HET) is the most studied effect involved in Au NRs-mediated photoredox catalysis. With the absorption of a photon ($h\nu$), a nearly free electron of the Au NRs can be elevated from the Fermi level (E_f) to a higher energy level (E_{sp}). This high-energy electron (i.e., hot electron) will lose energy through electron-electron scatting in about 10–100 fs [22]. During this excitation and energy redistribution process, a portion of hot electrons may transfer to a nearby acceptor, which can be a metal, semiconductor or reactant molecule. When the acceptor is a semiconductor, the SPR-excited hot electrons can inject into the conduction band (CB), as depicted in Fig. 3a. Thus, in this HET mechanism, the role of Au NRs is to act as a photosensitizer, which can expand the light response region of semiconductors. It can be inferred from the detailed description of the HET process that the fraction of excited hot electrons determines the hot electron injection efficiency. Thus, the size and shape of Au NRs, as well as the electrochemical properties of neighboring semiconductors play important roles in affecting the hot electron injection.

The environmental temperature is a critical parameter for redox reactions. Under the irradiation of light, chemical reactions can benefit from the increasing temperature around catalysts due to photothermal conversion [4,56,57]. When Au NRs-based nanostructures are employed as the catalysts in redox reactions, plasmonic photothermal conversion can generate heat on the catalysts and induce a local temperature increase, usually followed by heat transfer to the environment such as reactant molecules and solution [22,58,59]. The photothermal efficiency have strong correlations with the shape and size of nanostructures [60]. As mentioned above, the excited plasmons can decay through two routes: direct transfer of the energetic charge carriers to the nearby acceptors and local heating by converting the carrier energy into the phonon modes (process 3 and 4 in Fig. 2f, respectively). Given the short time scales of hot charge carriers transfer (<1 ns) and electron-phonon scattering (<10 ps), the heterointerfaces of hybrid structures should also be precisely controlled so as to maneuver the photothermal conversion during the plasmons decay [22,59].

Another proposed mechanism for Au NRs-mediated photoredox catalysis is ascribed to the promotion of an enhanced LEF near the surface of Au NRs, as illustrated in Fig. 2f (process 5 and 6). More specifically, the plasmonic Au NRs produce an intense LEF by localizing the incoming photons with specific frequency near the surface. This enhanced LEF is orders of magnitude higher

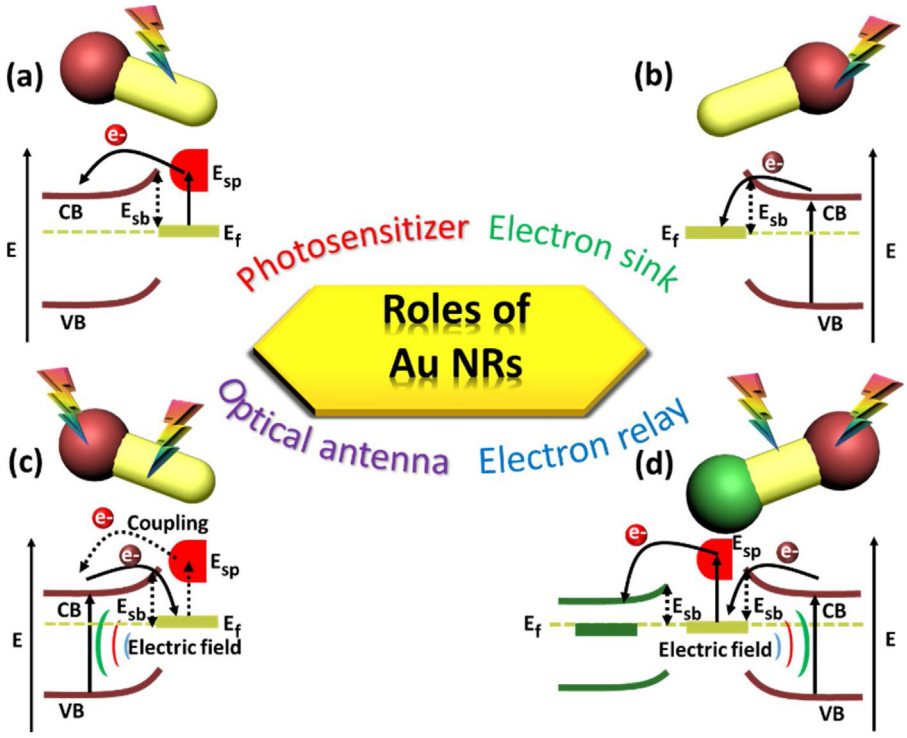

Fig. 3. (a–d) Schematic presentation of the charge transfer processes in Au NRs-based heterostructures under different illumination conditions. (a) Under photoexcitation of Au NRs. (b) Under photoexcitation of semiconductors. (c and d) Under simultaneous photoexcitation of both Au NRs and semiconductors.

than the field of incident photons, which means that the photon absorption rate of semiconductors located within the field enhancement regions should be significantly improved, since the formation rate of electron-hole pairs in the semiconductors is proportional to the square of the local intensity of the electric field [23,61,62]. Therefore, when a semiconductor is brought close to a photoexcited Au NR, the electron-hole generation rate in the semiconductor will be remarkably enhanced, thus increasing the photoactivity. The enhanced LEF can also benefit the photoredox reactions through dipole-dipole interaction (process 6 in Fig. 2f), in which the energy of a plasmonic oscillation is transferred from Au NRs to a semiconductor to promote electron-hole pairs generation and separation through an electric field [15,54]. This effect is also described as plasmon-induced resonant energy transfer (PRET) in some works [15,63]. In contrast to HET, where minimal separation (<2 nm) between the Au NRs and semiconductors is essential, LEF enhancement effects can still work in the present of any insulating interlayer, such as SiO_2 [64]. The efficiency of electric field promoting effect is affected by the spatial distance between the semiconductors and the Au NRs, as well as the spectral overlap between the intrinsic photoabsorption of semiconductors and the SPR absorption bands of Au NRs.

Charge transfer processes in Au NRs-mediated photoredox catalysis

When Au NRs are coupled with the semiconductors or other functional components to form the heterostructures, two possible phenomena may occur at the heterointerface under light irradiation: SPR excitation and Schottky barrier (E_{sb}) formation. As noted above, SPR effects promote the photoredox catalysis in three ways: HET, photothermal conversion, and LEF enhancement, while Schottky barrier can improve the photoactivity by trapping and prolonging the lifetime of electrons [8,65]. Although both phenomena have been well grounded throughout the research field, one crucial ambiguity still exists based on the proposed mechanisms. Specifically, what is the direction of charge flow? In this section, we will discuss the intricate relationships between the Schottky barrier and SPR excitation in the matter of affecting charge flow in Au NRs-based heterostructures, and the corresponding roles of Au NRs played in different charge transfer processes will be highlighted.

From the literature reports, it has been revealed that the Au NRs-based photoredox catalysis systems can be broadly classified in two categories, according to the modes of photoexcitation. Taking the Au NRs-semiconductor heterostructure as an example, in the first case, either semiconductor or Au NR component is photoexcited (Fig. 3a and b). The charge carriers are initially transferred from photoexcited component to other part of the composite material, which then induce the catalytic process. With visible light irradiation, the heterostructures combining wide bandgap semiconductors such as TiO_2 with plasmonic Au NRs fall in this category, where the hot electrons with energy higher than Schottky barrier inject from Au to the semiconductor TiO_2 to initiate the catalytic reactions [66–69]. This process is known as SPR-sensitization. A possible electron transfer from the surface plasmon state (E_{sp}) of Au NRs to the CB of semiconductors is schematically shown in Fig. 3a. For a particular case with exclusive photoexcitation of semiconductors, the excited electrons are flowing from the semiconductors and then trapped by the Au NRs due to the lower work function of Au [70,71]. A schematic presentation of such electron flow is shown in Fig. 3b, in which the Au NRs serve as electron sinks that capture the photoexcited electrons in the CB of semiconductors, resulting in an efficient spatial separation of charge carriers and prolonging the lifetime of the electrons for the redox reactions [8,65]. In this case, the presence of Schottky barrier can prevent the electrons from the Au NRs drifting back to the semiconductors.

Another possibility is that the Au NRs and semiconductors are both photoexcited (Fig. 3c and d). Composite materials, where the Au NRs are coupled with narrow bandgap semiconductors such as CdS, MoS_2, Cu_2O, and so forth, remain in this category [63,72–74]. The electron transfer process becomes more complicated in this situation. Even though most of the reports have predicted that the

photoexcited electrons are transferred from the excited state of semiconductors to the Au NRs [75], a recent study on Au-CdS NRs has showed that, the electron transfer in both ways (i.e., from CdS to Au or from Au to CdS) is possible [76]. In addition, the electron-hole pairs photogenerated from semiconductors can further interact with the plasmons or electric field of Au NRs [73]. Summarizing all the possible processes in this category, we show the charge carrier transfer protocols in Fig. 3c. Here, the Au NRs serve as optical antennas to provide energetic hot electrons and enhance LEF which can assist in generating and separating of the charge carriers. However, the competition between injection of hot carriers from Au NRs to semiconductors and charge transfer driven by the electron sink effect (i.e., from semiconductors to Au NRs) would reduce the Schottky barrier and the efficiency of charge trapping on Au NRs [77,78]. Introducing the third functional component as the electron accepters of Au NRs might be a promising strategy to solve this problem. As shown in Fig. 3d, Au NRs pose as electron relays to facilitate the charge transfer between different functional components. The matched band alignment and the formation of Schottky barrier in these Au NRs-based heterojunctions are favorable for steering the HET from Au NRs to semiconductors while suppressing the backflow of injected electrons from semiconductors to Au NRs [79]. Thus, when analyzing the electron transfer processes in Au NRs-semiconductor heterostructures, it is observed that the electrons can transfer from Au NRs to semiconductors or vice versa, which depends on the compositions and band alignment of the heterostructures as well as the light excitation source.

Fabricating, classifications and properties of Au NRs-based hybrids

The synthetic routes of Au NRs have been well established and described in several reviews [24,80–83]. There are three main routes to synthesize Au NRs, including electrochemical/photochemical method [84,85], template method [86,87], and seed-mediated growth method [25,88]. Readers who are interested in the synthesis of Au NRs can further refer to these works. In this section, we concentrate on the preparative methods and structural characteristics of different Au NRs-based heterostructures. According to the geometrical configuration of the heterostructures, Au NRs-based hybrids can be divided into four categories: (1) core@shell structures; (2) yolk/shell structures; (3) Janus structures; (4) supported Au NRs-based hybrid structures. In the past few years, several methods have been developed to control the size, morphology and crystalline phase of Au NRs-based composites, which can be generally classified into two groups, i.e., in-situ and ex-situ synthesis procedures.

Core@shell structures

In-situ growth approach has been considered as one of the effective methods to synthesize Au NRs-based composites with core@shell, yolk/shell or Janus morphology (Fig. 4a). Generally, the Au NRs, surface-capping agent and the soluble precursor of functional components (e.g., semiconductors, metal or metal-organic-framework materials) are mixed together in a certain solvent. Followed by hydrothermal/solvothermal [89,90], hydrolysis [91–93], thermal decomposition [94,95], cation exchange or chemical reduction treatment [96–98], the precursors can be transformed into specific nanostructures anchored on the Au NRs surface forming the hybrid structures (Fig. 4a). Au NRs-based core@shell hybrids with the maximum interface interaction between Au NRs and functional components, have led to fascinating properties especially in optics, catalysis, solar cell, and biotechnological applications [23]. By encapsulating Au NRs with a shell, it is possible to prevent aggregation, avoid undesirable corrosion, enhance thermal stability and strength interfacial electron transfer of the composites [99,100].

As shown in Fig. 4b-g, the development in nanotechnology enables the production of Au NRs@metal [101,102], Au NRs@semiconductor [89,93,94], Au NRs@insulator [103], and Au NRs@metal-organic-framework material (MOF) composites [58,104,105] with a wide range of size and shape tunable properties. Many studies have performed on coating semiconductor TiO_2 onto Au NRs through in-situ growth approach. Mainly three types of TiO_2 precursors, including inorganic titanium (III and IV) salt, organic titanium (IV) alkoxides and titanium (IV) complexes, have been used in these coating experiments [91,106–108]. Delicate control of the synthetic conditions, such as the type of precursors, the hydrolysis and condensation rates, can result in coating the TiO_2 shell with desirable thicknesses on Au NRs and good dispersibility of the obtained Au NRs core@TiO_2 shell nanostructures. Compared with Au NRs@metal oxide nanostructures, the synthesis of Au NRs@metal sulfide nanostructures with crystallization, composition and morphology control still remains a challenge because of the large lattice mismatch between the two components [109]. Taking advantage of the non-epitaxial growth enabled better crystallinity engineering under large lattice mismatch and cation exchange enabled precise control of stoichiometry, Zhang and co-workers have integrated plasmonic Au NRs and plasmonic nonmetallic $Cu_{2-x}S$ to form Au@$Cu_{2-x}S$ core@shell nanostructures with flexible shape, crystallization, and composition tailoring [110]. As shown in Fig. 4h, Au@CdS nanostructures with single-crystalline CdS shell are firstly synthesized by in-situ conversion of Ag shell on Au NRs core to amorphous Ag_2S and then to CdS shell by efficient tributylphosphine-initialized cation exchange synthetic chemistry. Then starting from the Au@CdS, the cation exchange between Cu^{2+} and CdS shell is controlled to obtain Au@$Cu_{2-x}S$ hybrids.

Yolk/shell structures

Au NRs-based yolk/shell structures can be considered as a special kind of core@shell architectures [100]. The major difference is the void between Au NRs core and shell in yolk/shell structures. Hence, some properties of yolk/shell structures are the same as core@shell structures. In addition to the commonality, Au NRs-based yolk/shell structures also have some unique characteristics. First, since the inside Au NRs core is isolated and has less contact with the outside hollow shell, any contact interference from the shell is minimized [109]. As a consequence, yolk/shell structures are excellent for modeling the catalytic properties of Au NRs, especially when the shell is an inert material such as SiO_2 [100]. Furthermore, because of the detachment from outside shell, the internal Au NRs core can provide more exposed active sites for catalytic reactions [110]. Second, the hollow shell is normally porous, which increases the accessibility of reactants to the Au NRs core and reduces the diffusion resistance of the products out of the space [111]. Third, it has been proved that the yolk/shell systems own the multiple light reflection ability between core and shell [109], which thereby can optimize the optical utilization of Au NRs.

The hard template method is an effective approach to synthesize the Au NRs-based yolk/shell materials. SiO_2 has been widely used as a hard template to synthesize yolk/shell nanostructures [112–114]. Typically, SiO_2 was firstly coated on the surface of Au NRs cores to form the core@shell nanostructures. Next, a semiconductor shell was deposited on the surface of core@shell composites through the hydrolysis or thermal decomposition of precursors. Lastly, NaOH or HF solution was added to remove the SiO_2 layer and form the Au NRs-based yolk/shell structures (Fig. 4a) [115]. In addition to this, recently developed sacrificial template method, in which the template is also used as the precursor of second func-

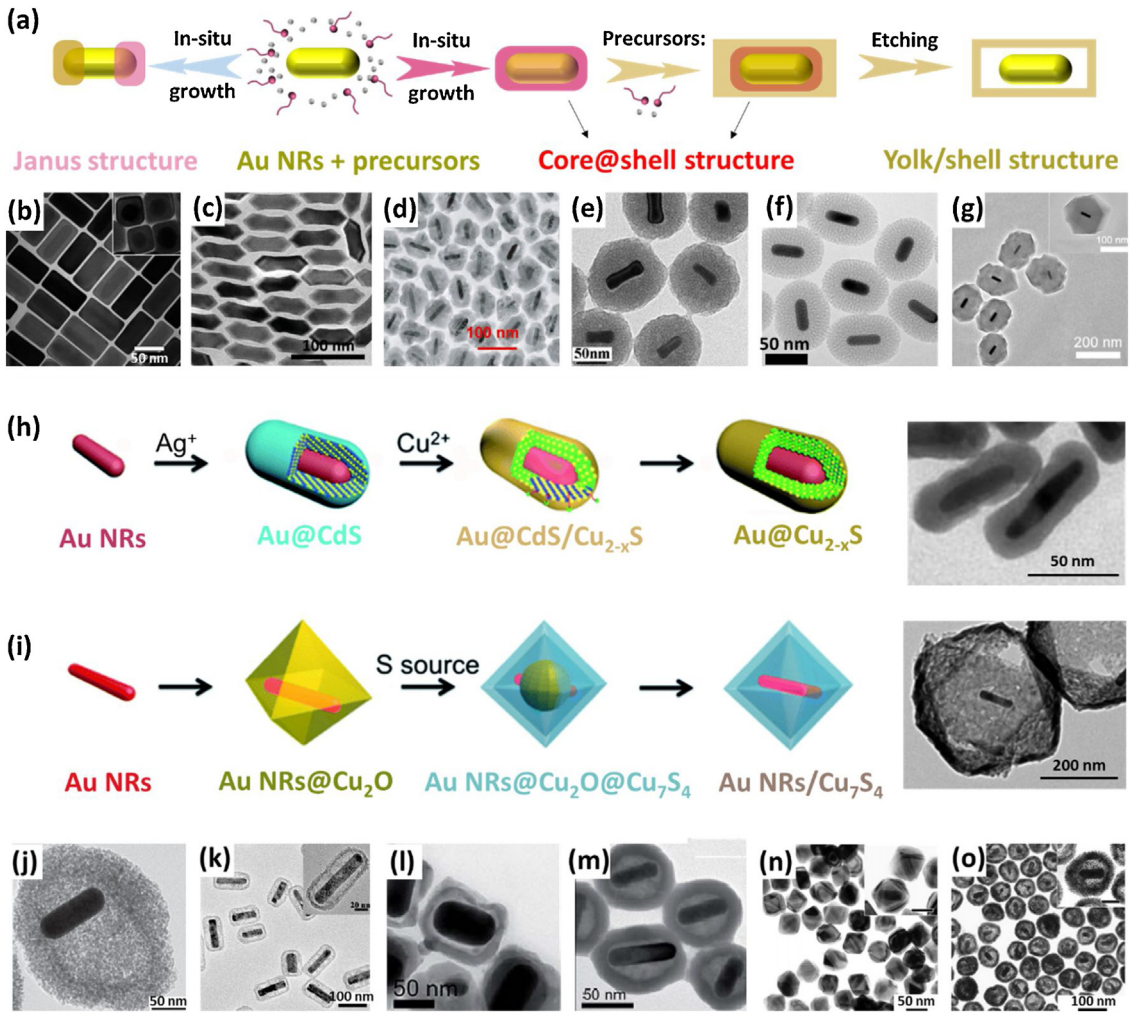

Fig. 4. (a) Scheme of synthesizing the core@shell, yolk/shell and Janus Au NRs-based hybrid by in-situ growth method. (b–g) Transmission electron microscopy (TEM) images of (b) Au NRs@Ag, (c) Au NRs@AuAg with AuAg alloyed shell, (d) Au NRs@CdS, (e) Au NRs@ZnO, (f) Au NRs@SiO_2 and (g) Au NRs@MOF nanostructures. (h and i) Schematic illustration of the synthesis route for (h) core@shell Au@$Cu_{2-x}S$ and (i) yolk/shell Au/Cu_7S_4 hybrid based on the in-situ growth method. The TEM images in (h and i) are corresponding to the targeted samples. (j–o) TEM images of (j) Au NRs/TiO_2, (k) Au NRs/$NaYF_4$, (l) Au NRs/CdS, (m) Au NRs/Nd_2O_3, (n) Au NRs@Ag and (o) Au NRs/Pt. (b) Reprinted with permission from [101]. Copyright 2011, Royal Society of Chemistry. (c) Reprinted with permission from [102]. Copyright 2015, Wiley. (d) Reprinted with permission from [89]. Copyright 2012, Wiley. (e) Reprinted with permission from [94]. Copyright 2013, Royal Society of Chemistry. (f) Reprinted with permission from [103]. Copyright 2014, American Chemical Society. (g) Reprinted with permission from [54]. Copyright 2018, Springer. (h) Reprinted with permission from [110]. Copyright 2016, Wiley. (i) Reprinted with permission from [117]. Copyright 2016, American Chemical Society. (j) Reprinted with permission from [112]. Copyright 2015, Wiley. (k) Reprinted with permission from [114]. Copyright 2012, Wiley. (l) Reprinted with permission from [109]. Copyright 2018, Royal Society of Chemistry. (m) Reprinted with permission from [118]. Copyright 2018, Royal Society of Chemistry. (n and o) Reprinted with permission from [121]. Copyright 2010, Wiley.

tional component, has also been attempted in the synthesis of Au NRs-based yolk/shell structural materials [116,117]. For example, Au NRs/Cu_7S_4 octahedral yolk/shell structures have been prepared through a sacrificial template method based on the Au NRs@Cu_2O core@shell nanostructures [117]. As shown in Fig. 4i, the Au NRs are primarily used as seeds for the preparation of Au NRs@Cu_2O core@shell NPs through an in-situ nucleation of Cu_2O on the surface of Au NRs in the aqueous solution. Then, the surface of Au NRs@Cu_2O template is sulfurized into Cu_7S_4 shell based on an inward replacement strategy. The residual Cu_2O is removed by HCl, resulting in the formation of Au NRs/Cu_7S_4 yolk/shell NPs. Fig. 4j, k and l disclose the typical Au NRs-based yolk/shell structures prepared by hard template method and sacrificial template method, respectively. The samples obtained by the former method usually have well-defined interface and composition.

A series of Au NRs-based yolk/shell structures have also been created by Ostwald ripening [118–120]. For example, Wang et al. have prepared Au NRs/Nd_2O_3 yolk/shell structural composites (Fig. 4m) by a simple hydrothermal method [118]. During this process, tiny Nd_2O_3 nanocrystallites are firstly assembled into solid shell. Then, the loosely packed crystallites on the outer surface of the particles serve as seeds for the re-crystallization process. With the consumption of the crystallites from the inner layers and the formation of re-crystallized shell, a void is formed. This empty space divides the particles into the core and the shell. Galvanic replacement reactions provide a versatile route to fabricate Au NRs/metal composites with controllable yolk/shell structures [121,122]. The key step of this process involves the replacement reaction between a suspension of nanoscale metal template and a salt of less active metal [115]. By means of galvanic replacement with other noble metals, the Au NRs@Ag core@shell solid nanocrystals (Fig. 4n) can successfully transform into yolk/shell structures with the Au NRs encapsulated inside a hollow Au, Pt or Pd nanocage (Fig. 4o) [121].

Janus structures

Janus structures, a special kind of material which integrates two or more components at small junctions and exposes other

regions, offer great opportunities for creating synergistic functions [17,123,124]. The peculiar properties of Janus structures, derived from their asymmetric structure, allow for their controlled self-assembly and surface activity [123]. Janus Au NRs/semiconductor (or metal) structures possess excellent catalytic activity, because the direct exposure of the Au NRs core and semiconductor shell to reactants on one side endows rapid transfer and separation of charge carriers at Au NRs/semiconductor, Au NRs/solution and semiconductor/solution interface [91,92]. Meanwhile, due to the protection from the semiconductor coating on the other side, Janus structures also show long-term stability in comparison with bare Au NRs [125–127].

Since the concept described by Gennes [128], various efforts have been focused on fabricating different kinds of Janus structures. Common strategies used to achieve the Janus heterostructures include site-selective nucleation or etching [129–131], direct epitaxial growth [132,133] and nonepitaxial growth [91]. The second functional component involved in Au NRs-based Janus nanostructures mainly include metals [134,135], metal oxides [91,92] and chalcogenide semiconductors [129,136]. Han et al. have reported the Au NRs-TiO_2 heterostructures with controlled geometry [91]. In their work, short and long Au NRs were firstly synthesized using seed-mediated growth method. Then, TiO_2 was grown anisotropically on one side of the NRs by controlled hydrolysis of titanium diisopropoxide bis(acetylacetonate) because of its slow hydrolysis rate (Fig. 5a). It is worth mentioning that the amount of the titanium precursor and the addition manner are very critical for the shape of the finally obtained nanostructures. By precisely controlling these two factors, Janus Au NRs/TiO_2 structures can be produced. Galen and co-workers have found that the spatial selectivity of the TiO_2 deposition on the Au NRs can be controlled by engineering the surface chemistry of Au NRs [92]. Anisotropic overgrowth of TiO_2 on the Au NRs tips was achieved by using cetyltrimethylammonium bromide (CTAB) as soft template, because bilayers of CTAB surface-capping agents are more densely packed on Au NRs sides than at the tips (Fig. 5b–d). In contrast, sodium dodecyl sulfate (SDS) or similar surfactants modified Au NRs have a more random molecular assembly on them, resulting in homogeneous overgrowth of TiO_2 on Au NRs (Fig. 5e). This property has also been utilized for the anisotropic overgrowth on CTAB-capped Au NRs with metal heterostructures [135,137].

In addition, Zhang et al. have demonstrated a versatile method for generating Janus Au-AgCdSe hybrid NRs with well controlled morphology and symmetry [136]. The synthesis mainly involves deposition of Ag tips at the ends of Au NRs seeds, followed by selenization of the Ag tips and overgrowth of CdSe on these sites. By simply manipulating the pH value of the system, the AgCdSe can selectively grow at one end, at both the ends or on the side surface of Au NRs, generating a mike-like, dumbbell-like, or toothbrush-like hybrids, respectively (Fig. 5f). These three types of Au-AgCdSe hybrids displayed distinct localized SPR and photoluminescence enhancement properties, demonstrating an effective pathway for maneuvering the optical properties of nanocrystals.

Supported structures

The ex-situ synthesis procedure has been widely used to fabricate Au NRs-based hybrids with supported structures due to its simplicity and operability. In the ex-situ synthesis procedure, the pre-synthesized semiconductors (or other functional components) with different morphology are mixed with the Au NRs to prepare Au NRs-semiconductors composites, as illustrated in Fig. 6a. The interfacial area has great influence on the properties of composites. Au NRs decorated semiconductors provide only a 1D-based interfacial interaction between them, which leaves the majority of the Au NRs surface uncovered [138,139]. In order to harness the unique physiochemical properties of Au NRs more effectively, the surface functionalization of individual counterparts is often required to enhance its solvent processability, stability and strengthen the spatial interaction between Au NRs and functional components [139–141]. For instance, Majima and co-workers have developed a novel plasmonic surface heterojunction composite by integrating Au NRs with $La_2Ti_2O_7$ nanosteps (Au-LTO NSP) [141]. The synthesis procedures of the composites based on a facile self-assembly approach are schematically shown in Fig. 6b. Au NRs samples are prepared through seed-mediated strategy and then attached on the mercaptopropionic acid (MPA)-functionalized $La_2Ti_2O_7$ nanostructures (LTO NSP) by ligand exchange for constructing Au-LTO NSP composites. The intermediate ligand of MPA can replace the original capping agent CTAB on Au NRs, facilitating a strong interaction between Au and LTO NSP through its thiol (-SH) and carboxylic (−COOH) groups. A final calcination can further strength the interfacial contact. As demonstrated in Fig. 6c and d, the Au NRs are well loaded on the step-structured LTO surfaces by the effective interfacial interaction.

The morphology of substrates is another key factor influencing the properties of supported Au NRs-based hybrid structures, as the SPR effects depend sensitively on the dielectric properties of the surrounding environment [23,142]. Sun et al. have argued that compared with 1D TiO_2 nanowires (NWs) counterpart, the hierarchical morphology on the three-dimensional (3D) surface of TiO_2 microspheres greatly increases the chance of reflected photons from all directions to re-contact with the Au NRs, and thereby stimulates the absorption of the incident photons on the surface of the 3D-based catalyst, which ultimately harvests a higher photon-electron and photo-thermal conversion efficiency [66]. Up to date, diverse substrates with different morphologies, such as zero-dimensional (0D) NPs [143,144], 1D NWs [79,138,145], two-dimensional (2D) nanosheets (NSs) [74,146–148] and 3D nanoarrays [149], nanoflowers [66,150] or nanospheres [151–153], have been used as the functional components to couple with Au NRs (Fig. 6a). Typical morphology of these composites is disclosed in Fig. 6e–j. These composites with various morphology oftentimes provide suitable substrates to incorporate with the third functional component, and thus more complex structures with desired property can be designed and synthesized [79,138].

Based on above descriptions, it is seen that we can control the structures, morphologies and properties of Au NRs-based hybrids by tuning the precursors, reaction time, temperature and surfactant in in-situ synthesis procedure, or simply adjusting the morphology and structure type of the pre-grown substrates in ex-situ assembling process. The in-situ preparation procedure is often more efficient than the ex-situ method to intimately integrate Au NRs with semiconductors or other functional components. Additionally, one-step synthesis through in-situ growth can produce the monodispersed hybrids, which is essential in researching the structure-property interplays of the samples. However, the specific virtue of ex-situ method should be given attention. For example, in the ex-situ assembling process, the size and morphology of the semiconductors in the composites can be retained almost the same as those of the initial forms [5,140]. This enables us to exclude the size and morphology effects when comparing the performance between blank semiconductors and Au NRs-semiconductors composites. Conversely, for the in-situ synthesized heterostructures, these effects cannot be eliminated due to the structural changes of semiconductor component in the composites in comparison to blank semiconductors, caused by the introduction of Au NRs during synthesis process, which can serve as the templates or supports to tune the structure of semiconductors [99,154].

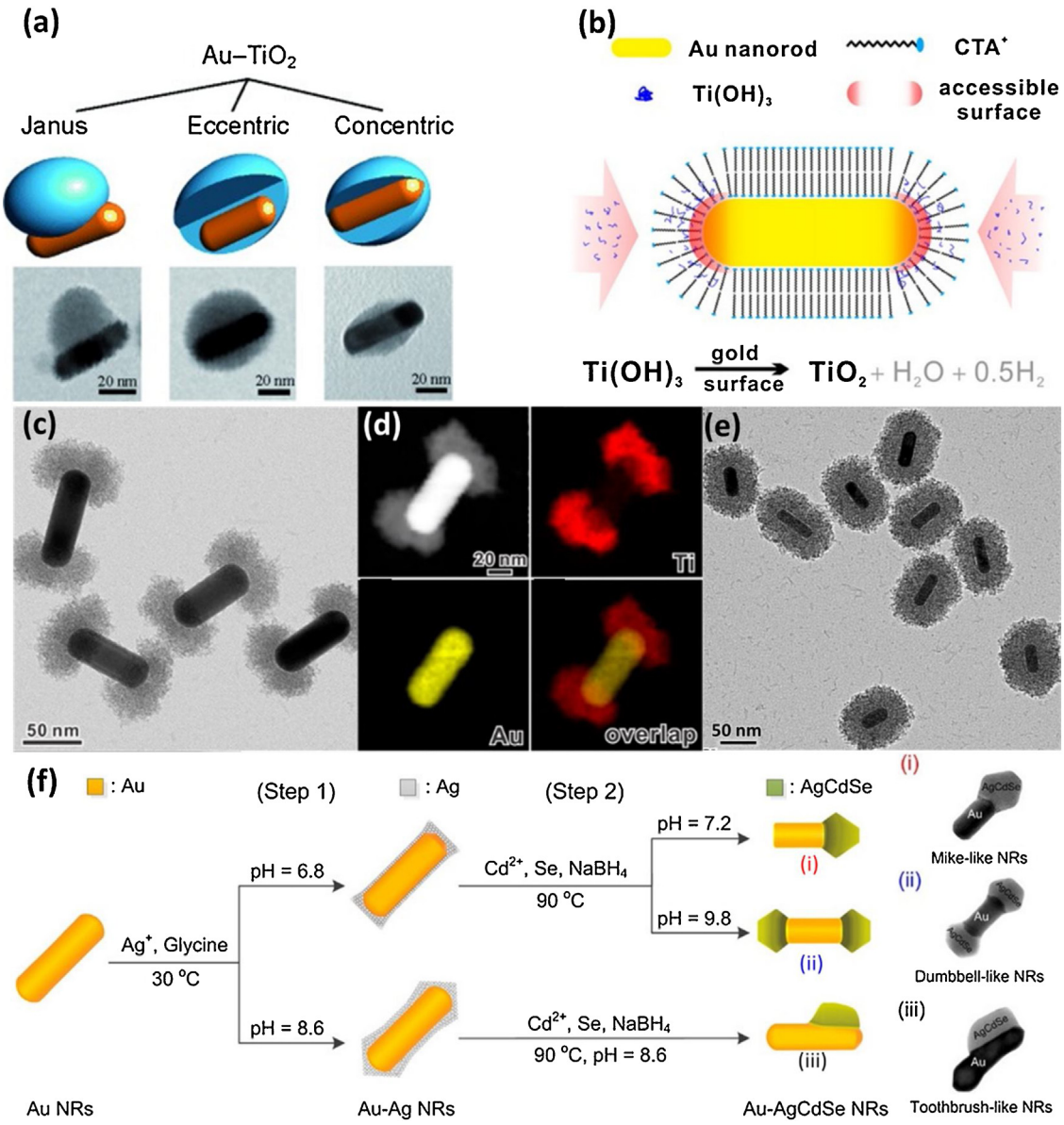

Fig. 5. (a) Schematic representations of the Au NRs-TiO_2 heterostructure with various geometries and corresponding TEM images. (b) Schematic showing the origin of anisotropic TiO_2 coating. (c) TEM image and (d) High-angle annular dark-field scanning transmission electron microscopy (HAADF-STEM) image and elemental map profiles of Janus Au NRs/TiO_2 prepared in the presence of CTAB as surfactant. (e) TEM image of core@shell Au NRs@TiO_2 prepared in the presence of SDS as the surfactant. (f) Schematic illustration of the syntheses of three different types of Janus Au-AgCdSe hybrids based on the in-situ growth method. (a) Reprinted with permission from [91]. Copyright 2011, Wiley. (b–e) Reprinted with permission from [92]. Copyright 2016, American Chemical Society. (f) Reprinted with permission from [136]. Copyright 2012, American Chemical Society.

Applications of Au NRs-based heterostructures in photoredox catalysis

Solar energy is an inexhaustible and economical clean energy source [1–5,8,9]. The use of sunlight to drive chemical reactions (i.e. photoredox catalysis) is one of the new approaches that can be potentially applied to various industrial chemical processes and environmental remediation applications [100,155]. With recent advances in photoactive material design, catalysis reaction system optimization, and new emerging mechanisms, the photoredox reactions have been exploited in thermal-based and electrochemical catalysis [9,149,156]. Although the photothermal catalysis (PTC) and photoelectrochemical catalysis (PEC) are not the typical photocatalytic redox process based on photoelectric property of the catalysts (i.e. photoinduced catalysis, PIC), they are the assisted effects to activate the catalysts and reactants, facilitate the separation of photoinduced charge carriers and ultimately promote the related redox catalysis reactions [4,9–11]. To achieve more efficient solar light utilization, the photothermal and photoelectric effects induced/enhanced catalysis are very useful strategies. We have provided a comprehensive list in Table 1 including a range of shape-controlled Au NRs-based nanostructures employed in photoredox catalysis, which demonstrate tremendous progress in this field.

Typical photoinduced redox catalysis

The existing works are mainly focused on the applications of Au NRs-based materials in PIC reactions, including photocatalytic elimination of pollutants [118,145,157], photoinduced selective green synthesis [68,112,138] and water splitting for H_2 production [158,159]. Photocatalysis is considered as "advanced oxidation pro-

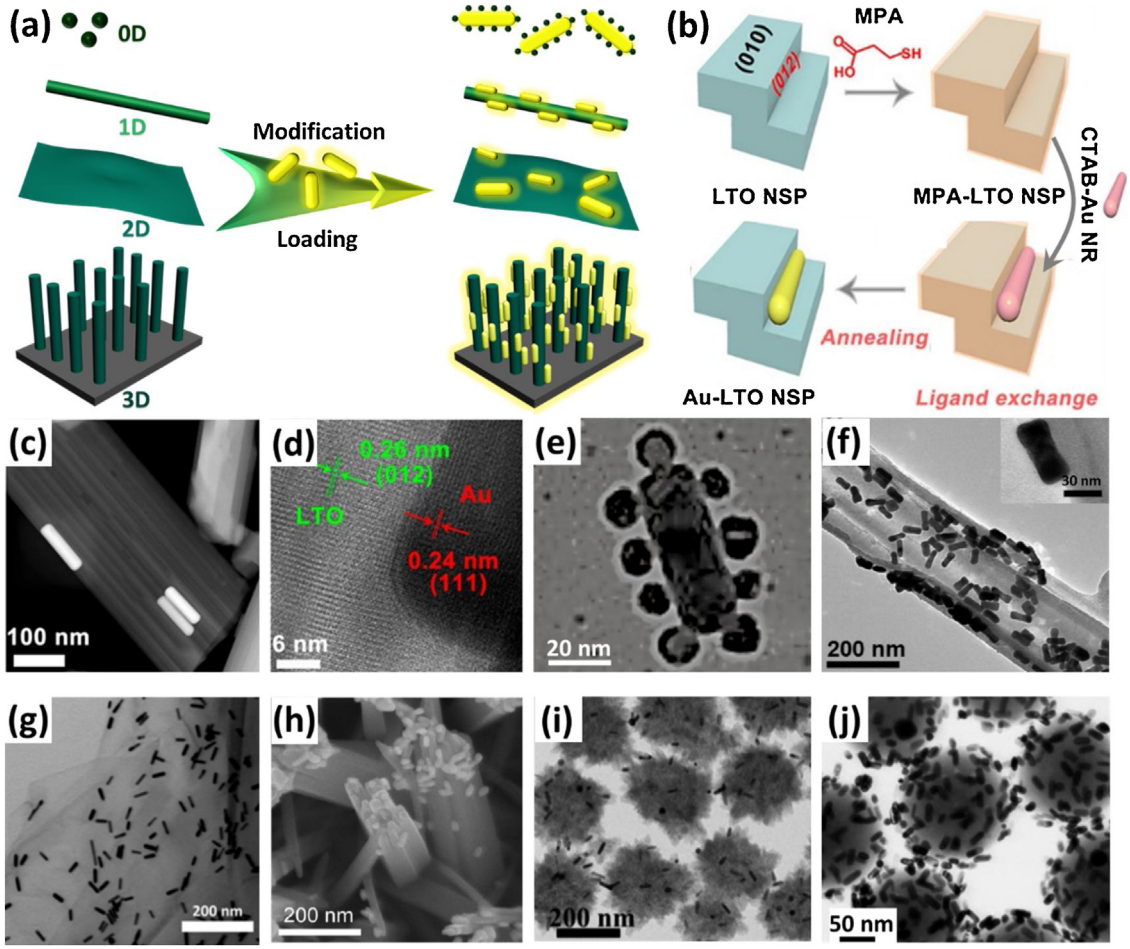

Fig. 6. (a) Schematic illustration of the preparation for Au NRs-based composites with supported structure by ex-situ synthesis procedure. (b) Schematic illustration of the preparation for Au-LTO NSP composites. (c and d) TEM images of Au-LTO NSP. (e–j) TEM or SEM images show the morphology of (e) 0D Au NPs supported on Au NRs, (f) 1D Si NWs supported Au NRs, (g) 2D GR NSs supported Au NRs and (h) 3D TiO_2 nanoarrays, (i) TiO_2 nanoflowers and (j) SiO_2 nanospheres supported Au NRs. (b–d) Reprinted with permission from [141]. Copyright 2018, American Chemical Society. (e) Reprinted with permission from [143]. Copyright 2013, American Chemical Society. (f) Reprinted with permission from [145]. Copyright 2011, American Chemical Society. (g) Reprinted with permission from [146]. Copyright 2013, Elsevier. (h) Reprinted with permission from [149]. Copyright 2013, American Chemical Society. (i) Reprinted with permission from [150]. Copyright 2017, Royal Society of Chemistry. (j) Reprinted with permission from [153]. Copyright 2004, Royal Society of Chemistry.

cess" because of its capability to generate reactive oxygen species (ROS), such as singlet oxygen ($^1O_2$), hydroxyl radicals ($^{\bullet}OH$) and superoxide anion radicals ($^{\bullet}O_2^-$) with strong oxidizability, which could be used for photocatalytic chemical oxidation and elimination of pollutants [9,93,160]. TiO_2 is one of the most important semiconductor that has been extensively studied for photocatalytic oxidation process, owing to its low toxicity, chemical and thermal stability, resistance to photocorrosion, and relative abundance [161]. However, pristine TiO_2 can only absorb UV light due to its large bandgap. To extend the photoresponse of TiO_2 to the visible and even NIR regions, many strategies have been developed, such as doping with metal or non-metal elements, introducing disorder, sensitizing with organic dyes, and coupling with other semiconductors [161–163]. For most of these methods, the photoresponse of TiO_2 can only be extended slightly to the visible region, and the obtained absorption coefficient in the extended spectral region is generally small [164]. Yet, plasmonic Au NRs nanocrystals that possess large absorption/scattering cross-sections in Vis-NIR region can strongly focus light close to the metal surface, thus expanding and enhancing the light absorption of TiO_2 in a broad-spectrum region [158].

In one example, Au NRs coated with a uniform TiO_2 nanoshell (Au/TiO_2) have been prepared by the ligand-assisted coating method [165], where a ligand exchange with an anionic polymer poly-styrene sulfonate (PSS) is firstly carried out to facilitate the Au NRs core contacting with the titanium (III) chloride precursor and induce a successful shell growth (Fig. 7a). This coating method can also be applied to Au nanospheres and other mono- and bi-metallic nanocrystals. UV–vis extinction spectrum indicates a distinct optical response of the TiO_2 coated Au NRs (NR/TiO_2) sample in 400–1200 nm range (Fig. 7b). The authors have employed the Au/TiO_2 to explore if they can function as photocatalysts for photobleaching of 9,10-anthracenediyl-bis(methylene) dimalonic acid (ABDA) under the L-SPR excitation (809 nm). To exclude the effect of the plasmonic photothermal conversion, the reactor is kept in a water bath maintained at room temperature. As shown in Fig. 7c, after 2 h of illumination, the absorption of ABDA rapidly decreases for Au/TiO_2 while that changes slightly for blank TiO_2, suggesting a large population of electron-hole pairs are generated under NIR light irradiation. The slight NIR light-driven photoactivity of blank TiO_2 may result from the structural defects.

In order to further improve the crystallinity of the TiO_2 coated Au NRs (Au NRs-TiO_2), Santamaria et al. have modified the above-mentioned synthesis method by supplementing a followed calcination procedure in air at 450 °C for 2 h [166]. In this case, the anatase TiO_2 shell with multiple nanocrystallites is formed (Fig. 7d). Bare Au NRs and Au NRs-TiO_2 are evaluated as photocatalytic enzyme-like glucose oxidase surrogates under NIR laser

Table 1
Summary of Au NRs-based nanostructures with tailored structures for photoredox catalysis.

Catalyst	Structure	Preparation	Application	Irradiation source	Ref.
Au NR/ZnO	Core@shell NP	In-situ hydrolysis	PIC elimination of ABDA	Ti:sapphire laser	[93]
Au-Pt@CdS	Core@shell NP	In-situ refluxing	PIC alcohol splitting	>420 nm	[212]
Au NR-TiO_2	Core@shell NP	In-situ coating	PIC oxidation of glucose	809 nm laser	[166]
Au NR@CeO_2	Core@shell NP	In-situ coating	PIC oxidation of BA	>420 nm, FSR[a]	[68]
GR-ZnO-Au NR	Supported NS	Ex-situ hydrothermal	PIC reduction of NB	UV light	[168]
Au NR@Cu_2O	Core@shell NP	In-situ epitaxial growth	PIC production of H_2	Simulated sunlight	[159]
Au-Pt-CdS	Core@shell NP	In-situ assembly	PIC production of H_2	AM 1.5, FSR	[73]
Pt/MIL-125/Au	Supported NP	Ex-situ assembly	PIC production of H_2	300-800 nm	[184]
Au NR-Fe_2O_3	Supported film	Ex-situ electrodeposition	PEC water splitting	AM 1.5	[173]
Au NR-TiO_2	Supported array	Electron beam lithography	PEC water oxidation	450-1150 nm, FSR	[174]
Au/TiO_2/Au	Supported cavity	Ex-situ assembly	PEC water splitting, PIC elimination of MB[b]	>405 nm, FSR	[175]
Au-TiO_2-Pt	Janus film	Electron beam deposited	PEC production of H_2	AM 1.5, FSR	[176]
Co/Au NR/TiO_2	Supported array	Electron beam evaporation	PEC water splitting	AM 1.5, FSR	[177]
Au-Pd	Janus NP	Seeded growth	PTC Suzuki coupling	809 nm laser	[137]
Pd-tipped Au NR	Janus NP	Seeded growth	PTC reduction of 4-NP[c], dehydrogenation of FA[d]	>460 nm, FSR	[182]
Au NR-TiO_2	Yolk/shell NP	In-situ template method	PIC BA oxidation	>420 nm	[112]
Pd-covered Au NR	Core@shell NP	Seeded growth	PTC reduction of 4-NP, dehydrogenation of FA	>460 nm, FSR	[182]
Au-Pd	Core@shell NP	Seeded growth	Styrene hydrogenation	>400 nm, FSR	[59]
Au NR@ZIF-8	Core@shell NP	In-situ assembly	PTC production of ROS	808 nm laser	[58]
Au/TiO_2	Core@shell NP	In-situ coating	PIC elimination of ABDA	809 nm laser	[165]
Pt@MIL-125/Au	Supported NP	Ex-situ assembly	PIC production of H_2	300-800 nm	[184]
Au@Pd	Core@shell NP	Seeded growth	PIC ROS production, PTC C-C coupling reaction	>510 nm	[22]
Au@Cu_2O	Yolk/shell NP	In-situ encapsulation	Conversion of n-hexene	N.A.[e]	[120]
Au@$Cu_{2-x}S$	Core@shell NP	Hydrothermal method	Water heating	700-2000 nm	[185]
Au-Metal sulfide	Core@shell NP	In-situ deposition	PIC elimination of RhB	N.A.	[194]
Au-TiO_2	Supported NP	Ex-situ deposition	PIC production of H_2	>420 nm, FSR	[193]
Au-TiO_2-Au	Supported array	Ex-situ assembly	PEC water splitting	300-900, FSR	[149]
Pt-tipped Au NR	Janus NP	Anisotropic overgrowth	PIC production of H_2	460-820 nm, FSR	[135]
Pt-covered Au NR	Janus NP	Anisotropic overgrowth	PIC production of H_2	460-820 nm, FSR	[135]
Au NR-CdS	Yolk/shell NP	Cation exchange reaction	PIC production of H_2	>400 nm	[109]
Au NR-TiO_2	Supported NP	Ex-situ assembly	PIC oxidation of IPA[f]	400-920 nm, FSR	[139]
CdS-Au	Supported array	Hard template methods	PEC production of H_2	AM 1.5	[198]
(MoS_2-TiO_2)/Au	Supported array	Drop-casting method	PEC production of H_2	Simulated sunlight	[199]
Au@Pd	Supported nanoarray	Seeded growth	PIC production of ROS,PTC C-C coupling reaction	>510 nm	[22]
Au-MoS_2	Supported film	Ex-situ assembly	PIC production of H_2	809 nm laser	[74]
Co-Au/TiO_2-Pt	Supported array	Atomic layer deposition	PEC water splitting	AM 1.5, FSR	[219]
CdS-Au NR	Supported NW	Ex-situ assembly	PIC production of H_2,nitrocompounds reduction	>510 nm, FSR	[138]
BP-Au-CdS	Supported NW	Ex-situ assembly	PIC production of H_2	Simulated sunlight, FSR	[79]
Au@Pt@CdS	Core@shell NP	In-situ refluxing	PIC alcohol splitting	>420 nm	[212]
Au NRs-TiO_2	Janus NP	In-situ anisotropic growth	4-NP reduction	N.A.	[91]
Au NR/TiO_2	Janus NP	In-situ anisotropic growth	PIC production of H_2, elimination of MB	Visible light	[92]
Au/CdSe	Janus NP	Cation exchange reaction	PEC production of H_2	>420 nm, FSR	[220]
Au-$La_2Ti_2O_7$	Supported NSP	Ex-situ assembly	PIC production of H_2	>420 nm, FSR	[141]
Au/Ag NRs-Si	Supported NW	Ex-situ assembly	PIC degradation of NB	N.A.	[145]
TiO_2/Au NR	Supported NP	Ex-situ assembly	PIC degradation of RhB	420-780 nm	[150]
Au@PtAg@ZIF-8	Core@shell NP	In-situ assembly	PIC reduction of CO_2	200-1000 nm	[105]
$Bi_4Ti_3O_{12}$-Au	Supported NS	Ex-situ assembly	PIC pollutants degradation	Visible light	[118]
Au NR-Cu_7S_4	Janus NP	Ix-situ hydrothermal	Photothermal conversion	808 nm laser	[221]
Au NR/ZnO	Supported NP	Ex-situ assembly	PIC degradation of RhB, PEC water splitting	200-1100 nm	[152]
TiO_2/Au	Supported NP	Ex-situ assembly	PIC production of H_2	Simulated sunlight	[222]
AgTiO_2-Au NR	Supported NP	Ex-situ assembly	PIC production of H_2	>550 nm	[158]
Au NR/Ag_3PO_4	Supported NP	Ex-situ co-precipitation	PIC degradation of RhB	>420 nm, FSR	[223]
Au NR@Fe_3O_4	Core@shell NP	In-situ hydrolysis	PIC elimination of ABDA	>470 nm	[224]
Au/TiO_2	Supported NP	Ex-situ assembly	PTC degradation of RhB	420-780 nm	[66]
Au-CdS	Supported NR	Ex-situ impregnation	PIC pollutants degradation	Direct sunlight	[157]
Au@Cu_2O	Core@shell NP	Epitaxial growth	PIC degradation of MO[g]	>400 nm	[72]
Au@Pd	Janus NP	Seeded growth	PIC production of ROS,PTC C-C coupling reaction	>510 nm	[22]
Au NR-MoS_2	Supported NS	Ex-situ assembly	PIC production of H_2	>460 nm	[147]
GR-Au NR	Core@shell NP	Ex-situ assembly	PIC reduction of CO_2	808 nm laser	[225]

[a] FSR refers to full spectrum response.
[b] MB refers to methylene blue.
[c] 4-NP refers to 4-nitrophenol.
[d] FA refers to Formic acid.
[e] N.A. refers to not available.
[f] IPA refers to 2-propanol.
[g] MO refers to methyl orange.

(808 nm) irradiation while keeping a constant reaction temperature of 32–34 °C with the aid of a thermostatic bath. Remarkably, the uncoated Au NRs show no significant formation of gluconic acid (Fig. 7e). In contrast, the Au NRs-TiO_2 photocatalyst with the core@shell configuration progressively converts glucose into gluconic acid. However, the selectivity toward gluconic acid is not very satisfactory in this reaction system (Fig. 7f). This may be due to the formation of nonselective $^{\bullet}OH$, which has strong oxidation capacity to mineralize organic compounds (Fig. 7g) [160]. To avoid the production of $^{\bullet}OH$, some organic molecules such as acetonitrile and benzotrifluoride have been chosen as solvent for the selective photooxidation reactions [68,112,167]. For instance,

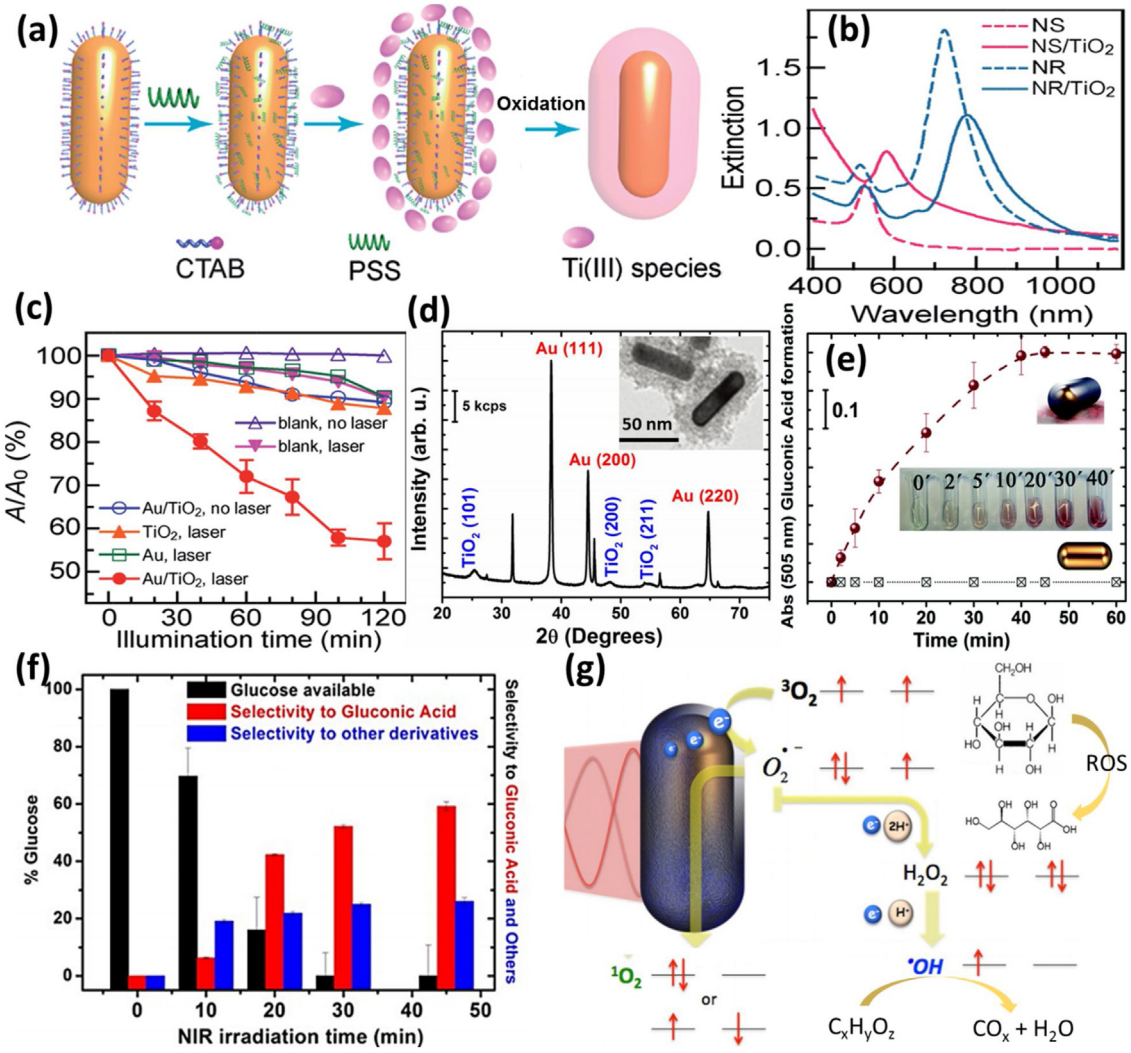

Fig. 7. (a) Schematic describing the coating of TiO_2 onto Au NRs to produce Au/TiO_2 nanostructures. (b) Extinction spectra of the Au NRs sample (NR) and the Au/TiO_2 core@shell nanostructure sample (NR/TiO_2). (c) Normalized reductions in the absorption of ABDA as functions of the illumination time. (d) X-ray diffraction (XRD) pattern of Au NRs-TiO_2 after calcination at 450 °C. Inset shows the TEM image of Au NRs-TiO_2. (e) The formation of the gluconic acid upon irradiation with a NIR laser at different time intervals and in the presence of the Au NRs and Au NRs-TiO_2. (f) Evaluation of the cumulative glucose conversion and selectivity towards gluconic acid and other oxidation products at different irradiation times. (g) Schematic plot describing likely routes for the NIR-induced generation and consumption of ROS species such as $\bullet O_2^-$, $^1O_2$ and •OH. (a–c) Reprinted with permission from [165]. Copyright 2014, Royal Society of Chemistry. (d–g) Reprinted with permission from [166]. Copyright 2017, Royal Society of Chemistry.

Yu's group has demonstrated that the Au NRs core@CeO_2 shell (Au NRs@CeO_2) nanostructures are an attractive type of photocatalysts for the selective oxidation of benzyl alcohol (BA) to benzaldehyde (BAD) with O_2 in acetonitrile [68]. Under the broad-band Vis-NIR ($\lambda > 420$ nm) light irradiation, the conversion and selectivity obtained with this core@shell nanostructures are superior to the blank CeO_2. The enhanced performance of the Au NRs@CeO_2 is derived from the synergistic effect between the Au NRs core acting as a plasmonic component for efficient light harvesting and the CeO_2 shell providing catalytically active sites for the oxidation reactions.

In the works mentioned above, the roles played by Au NRs in different photocatalysis systems are the Vis-NIR light-activated photosensitizers to sensitize the semiconductors. However, the photocatalytic efficiency over such systems is relatively low in contrast to those by semiconductor photoexcitation. To obtain higher photocatalytic activity, the structural design of special composite catalysts to synergistically integrate Au NRs-mediated enhancement mechanism and bandgap photoexcitation of semiconductors is desirable. Chang and co-workers have recently developed a highly active graphene (GR)-ZnO-Au NRs composites for photocatalytic reduction of nitrobenzene (NB) [168]. It is demonstrated that the contribution of Au NRs toward the photoactivity enhancement of ZnO is acting as an electron sink, which assists in efficient charge separation. As shown in Fig. 8a, under irradiation with UV light, a large number of free electrons in the CB and holes in the valence band (VB) are generated within ZnO. The electrons in CB of ZnO have work functions of -4.05 eV (vs. vacuum). On the other hand, the work functions of GR and Au are -4.42 and -4.70 eV (vs. vacuum), respectively. As a result, the electrons transfer rapidly from ZnO to GR and to Au NRs, minimizing electron-hole recombination, leading to rapid reduction of NB. A novel hot-dog (HD) structured Au NRs@Cu_2O has been designed and synthesized using Au NR as inner "sausage" and Cu_2O as outside "bread" to harness the plasmonic antenna and co-catalytic effect of Au NRs [159]. The HD structure is a kind of quasi-core@shell structure with intimate interfacial contact between Au NRs and p-type semiconductor Cu_2O (Fig. 8b), which could promote the holes transfer through Au NRs/Cu_2O interface, reducing the charge carriers recombination of the semiconductor, as depicted in Fig. 8c. In addition, the

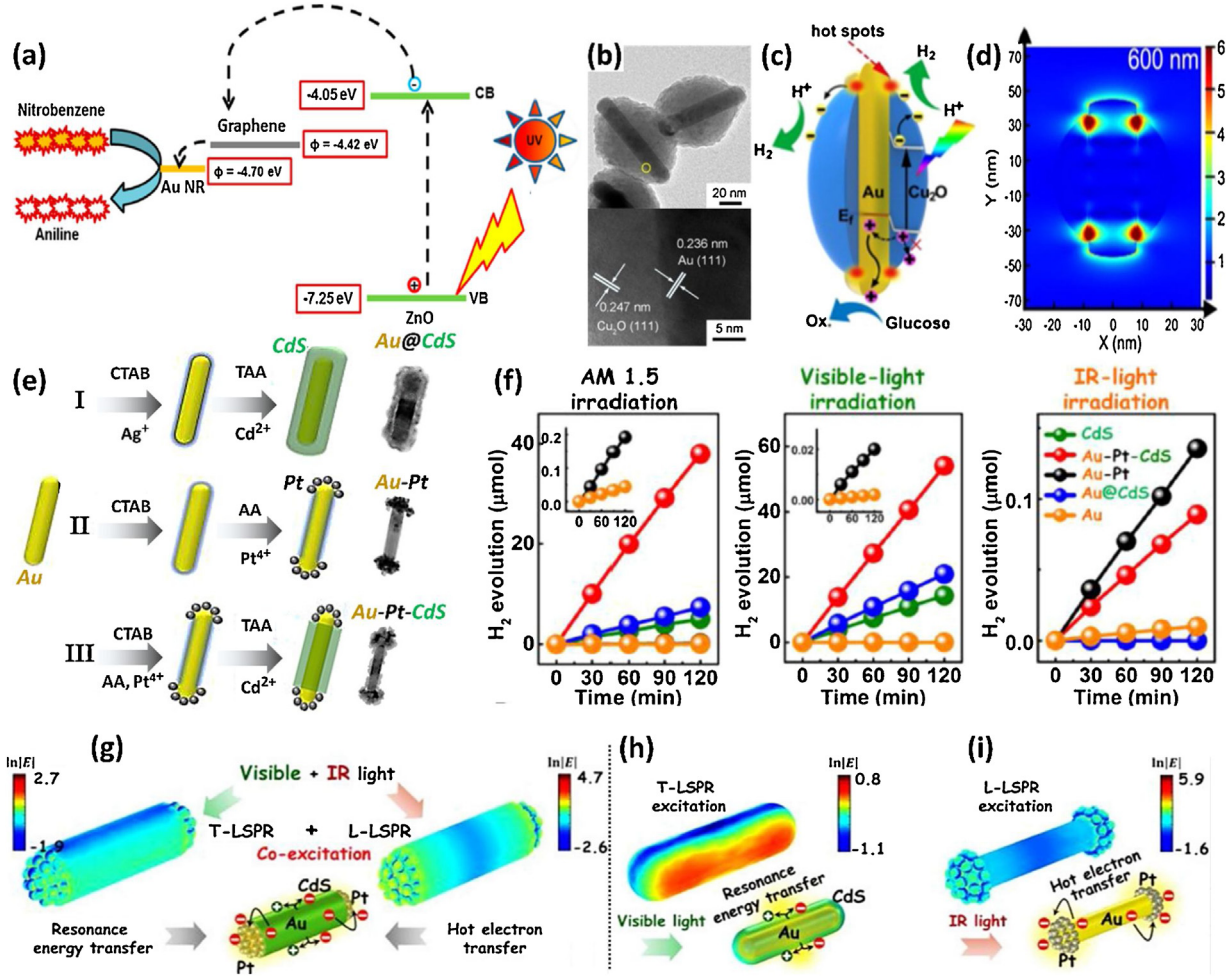

Fig. 8. (a) Schematic diagram showing the transfer of electrons from the different energy levels of the GR-ZnO-Au NRs for the photoreduction of NB. (b) TEM images of Au NRs@Cu_2O. (c) Schematic illustration of electron transfer in Au NRs@Cu_2O. (d) Simulated electric-field spatial distribution on the x–y plane for Au NRs@Cu_2O under 600 nm photoexcitation. (e) Synthesis routes and TEM images of the Au@CdS, Au-Pt, and Au-Pt-CdS. (f) Time-dependent photocatalytic H_2 generation plots of the as-synthesized samples under simulated sunlight (AM 1.5) irradiation, visible light irradiation and IR-light irradiation. (g–i) Simulated electric field distributions and the schematic diagrams of charge carriers transfer in (g) Au-Pt-CdS, (h) Au@CdS NRs and (i) Au-Pt under L-SPR and T-SPR excitation. (a) Reprinted with permission from [168]. Copyright 2013, American Chemical Society. (b–d) Reprinted with permission from [159]. Copyright 2017, Elsevier. (e–i) Reprinted with permission from [73]. Copyright 2018, Wiley.

head-exposed Au NRs exhibit strong SPR to extend the visible light absorption region and provide a strongly enhanced LEF at surface of photocatalyst to improve the transfer of electrons (Fig. 8d). The H_2 evolution rate of HD Au NR@Cu_2O shows 23.6 times improvement compared with that of pure Cu_2O due to these structural advantages.

Recently, Dong et al. have reported a novel plasmonic photocatalyst, where Au NRs work as electron relays, active photosensitizers and plasmonic antennas simultaneously [73]. The heterostructures are synthesized through selective assembly of the Pt and/or CdS nanostructures onto the Au NRs via a controllable multi-step wet-chemistry route (Fig. 8e). The H_2 generation rates over Au NRs-based materials under different irradiation conditions are shown in Fig. 8f. The photoactivity of Au-Pt-CdS is higher than that of Au@CdS, blank CdS and Au, no matter under simulated sunlight (AM 1.5), visible light or infrared (IR) light irradiation. They have demonstrated that the enhanced photoactivity of Au-Pt-CdS can be ascribed to the dual-resonance modes of anisotropic Au NRs, which induce a unique synergistic effect between the PRET and HET processes within the ternary Au-Pt-CdS heterostructure (Fig. 8g). More specifically, the T-SPR of Au NRs arising from the electron oscillations along the perpendicular direction of length axis, are overlapped with the interband absorption of CdS, which can induce the plasmonic PRET process for promoting the charge carriers generation and separation in the CdS component after visible light or simulated sunlight irradiation (Fig. 8h). The L-SPR originating from the electron oscillations in the length axis of Au NRs is the dominant channel for the generation and transfer of plasmonic hot electrons in the bimetal Au-Pt component (Fig. 8i). As such, upon simulated sunlight irradiation (both L-SPR and T-SPR are photoexcited, Fig. 8g), the photoactivity of Au-Pt-CdS is higher than that of the CdS by almost one order of magnitude. However, the H_2 generation rate of Au-Pt-CdS under IR light irradiation is still inefficient, which is even lower than that of Au-Pt due to the slow interfacial charge transportation across the semiconductor CdS (Fig. 8f). Further photoactivity improvement may be accomplished by engineering the ingredient composition and spatial distribution of semiconductor or the heterointerface between the Au NRs, Pt and semiconductor.

Photoelectrochemical catalysis

The concept of PEC has emerged as a result of an effort to mimic photosynthesis by coupling solar energy harvesting and electrochemical catalysis in a single device [169,170]. This approach provides a big step forward towards the conversion of solar energy to chemical energy by applying a small to no external bias [171]. A typical design of PEC system, which is initially presented in 1972 [172], is shown in Fig. 9a. The basic cell is composed of at least one

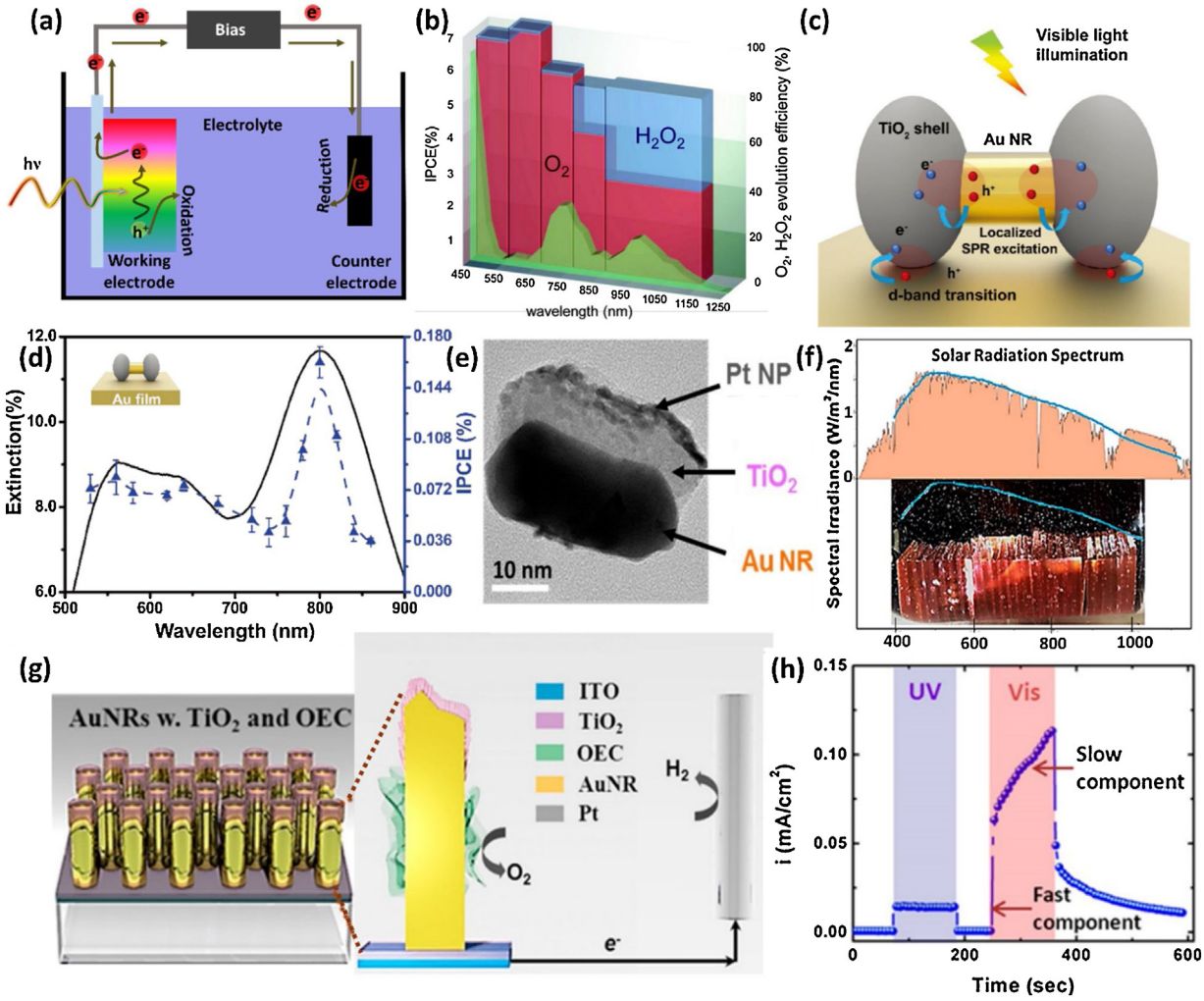

Fig. 9. (a) Schematic of a basic PEC cell including a photoanode and cathode that are immersed in an electrolyte and connected by an external electric wire. (b) Reaction yield of O_2 and H_2O_2 as a function of the wavelength ranges and its corresponding IPCE action spectrum. (c) Schematic of the hot carrier generation in Au/TiO_2/Au nanocavity through both SPR excitation and d-band transitions. (d) Measured IPCE for the Au/TiO_2/Au nanocavity system and their corresponding extinction spectra. (e) Representative TEM image of the Au-TiO_2-Pt Janus particle. (f) A digital photograph of H_2 bubbles rising above a tandem stack of multiple plates bearing Janus particles with different aspect ratios and illuminated with white light (AM 1.5). (g) Schematic of the Co/Au NRs/TiO_2 working cell for overall water splitting. (h) Photocurrent versus time plots for Co/Au NRs/TiO_2 PEC cell under visible ($\lambda > 410$ nm) or UV ($\lambda < 320$ nm) light irradiation. (b) Reprinted with permission from [174]. Copyright 2012, American Chemical Society. (c and d) Reprinted with permission from [175]. Copyright 2018, Wiley. (e and f) Reprinted with permission from [176]. Copyright 2015, American Chemical Society. (g and h) Reprinted with permission from [177]. Copyright 2012, American Chemical Society.

photoactive material or photoelectrode and a metal counter electrode that are immersed in an electrolyte and connected by external electric wire. Different from the typical PIC based on particulate system, the reduction and oxidation reactions in PEC system occur on the different electrodes separately.

The first Au NRs-based photoelectrode has been reported by Park et al., which is composed of the highly ordered and vertically grown α-Fe_2O_3 NRs arrays on an Au NRs substrate [173]. The composite electrode shows high photocurrent density (8 mA cm^{-2}) under 1 sun condition. Since then, many other Au NRs-based photoelectrodes with various components and structures have been reported. Misawa and colleagues have firstly demonstrated the feasibility of water oxidation using NIR light-responsive Au NRs arrays [174], which show two distinct SPR features at 1040 and 780 nm corresponding to the L-SPR and T-SPR modes, respectively. Under visible light ($\lambda < 750$ nm) irradiation, the main product arising from the photoanode is O_2, while for NIR window ($900 < \lambda < 1150$ nm), 58% of the resulting product is H_2O_2 (Fig. 9b). This result suggests the great promising for utilizing the plasmon-induced charge excitation under different irradiation conditions to regulate the charge transfer process and activation energy of the targeted reactions.

Au NRs has also been applied to photocathode systems that generate H_2 as the main product. Lei et al. have demonstrated that Au/TiO_2 dumbbell nanostructures assembled on a thin Au film (Au/TiO_2/Au) can serve as an efficient optical absorber and a hot carrier generator in the visible region [175]. Upon excitation of SPR in such coupled particle-on-film nanocavities, the energetic electrons in Au NRs can inject over the Au/TiO_2 Schottky barrier and migrate to TiO_2, participating in the proton (H^+) reduction reaction occurring at the TiO_2 surface (Fig. 9c). The incident photon-to-electron conversion efficiency (IPCE) result in Fig. 9d shows that the wavelength-dependent IPCE for the system follows the same trend as the extinction spectrum, which reveals the strong near-field coupling between the Au/TiO_2 and the Au film. To achieve a panchromatic light absorption across the entire Vis-NIR region, Moskovits and colleagues have utilized Au NRs of different aspect ratios to construct Au-TiO_2-Pt Janus particles assembled in a single photocatalytic device (Fig. 9e) [176]. The Au NRs harvest light to generate hot electrons, which then inject into the adjacent TiO_2 and transfer to the Pt NPs for H_2 evolution. By using a rational mix among the Janus particles with different aspect ratios ranging from 1.4 to 3.0, the absorption spectrum of the entire system (stacks of

quartz substrates) highly resembles that of the AM 1.5 solar spectrum (Fig. 9f). With methanol as the sacrificial electron donor, the device can operate for more than 200 h with a H_2 production rate of 2.3 μmol/h.

Fig. 9g shows the overall water splitting on a type of relatively complex hybrid nanostructures composed of Co oxygen evolution co-catalyst (OEC) and crystalline TiO_2 co-modified Au NRs (Co/Au NRs/TiO_2) [177]. Under simulated AM 1.5 solar irradiation, the Schottky interface between Au NRs and TiO_2 collects and conducts the hot electrons to an unilluminated Pt counter-electrode where H_2 gas evolves. The resultant positive charges holes in the Au NRs are extracted by the Co OEC for oxidizing water to O_2 gas. Notably, it is seen from the Fig. 9h that the solar-to-fuel production efficiency under visible light ($\lambda > 410$ nm) illumination is up to 20-folds higher than that with UV ($\lambda < 320$ nm) wavelength irradiation, indicating that 95% of the effective charge carriers derives from the SPR excitation of Au NRs. This is the first work to show the efficiency of plasmonic devices with visible light irradiation significantly in excess of that with UV light illumination.

In general, the PEC configuration provides great flexibility in designing and selecting photoactive materials [178]. The photoactive and catalytic materials can be fixed on the separate electrodes that are located in different chambers. Also, in a PEC cell, the Fermi level of the photoelectrode can be controlled via a potentiostat, and the redox reactions can be controlled at a desirable potential so that reaction selectivity can be improved [179]. However, from the perspective of applications, current utilization of Au NRs-based PEC catalysis is mostly immersed in water splitting. The applications in N_2 and CO_2 reduction, organic synthesis and recently developed electrocatalytic oxidative biomass upgrading integrated with H_2 production may require more exploration [180].

Photothermal catalysis

Based on above discussions, it can be seen that in typical PIC and PEC processes, the driving forces to catalytic reactions are the photogenerated electron-hole pairs. Being different from these two types of catalytic reactions, PTC proposed in this section refers to the photo-assisted catalysis process dominated by the photothermal effect of plasmonic metals with an additional photoactivation mechanism resulting from HET. Typical photothermal catalysis (without HET) has nothing different from conventional thermal catalytic reactions, except for the heating method [10,57]. By the flexible use of catalytic materials, photothermal catalysis can be an important supplement to photocatalysis and thermal catalysis for improving the efficiency of solar energy utilization, especially for low-energy photons [22,57,181]. Plasmonic Au NRs-based composites can effectively channel the flux of UV, visible, and especially NIR photons into heat to drive the catalytic reaction directly.

In the non-irradiative SPR decay, electrons in Au NRs with a non-thermal electron distribution will undergo a thermalization into a thermal Fermi-Dirac distribution. Then, cooling of the hot electrons occurs by energy transfer to the phonon modes, leading to an increase of temperature on the Au NRs (also called Ohmic damping) [10]. Therefore, if the energetic hot charge carriers are not involved in the charge transfer process in plasmonic photocatalysis, the energy of the SPR will finally dissipate into heat in the local environment to enhance the mass transfer and reaction speed. Pd is a well-known catalyst for many important organic synthesis reactions [98,127]. Some effective approaches have been developed to couple the light harvesting ability of Au NRs with the catalytic activation ability of Pd. For instance, Pd NPs deposited on the surface of Au NRs (Au-Pd) have been reported to efficiently drive Suzuki coupling reaction under light irradiation (Fig. 10a) [137]. The integration of plasmonic Au NRs with catalytic Pd NPs through seed-mediated growth enables efficient Vis-NIR light harvesting of the hybrid nanostructures (Fig. 10b). Under illumination with 809 nm laser at 1.68 W, the yield of the Suzuki coupling reaction is approximately 2 times as large as that obtained when the reaction was thermally heated to the same temperature (Fig. 10c). Moreover, the yield is also higher than that obtained from Au-TiOx-Pd nanostructures under the same laser illumination, where a 25 nm thick TiO_x shell is introduced to prevent the photoinduced catalysis process (Fig. 10c). These results indicate that the catalytic reactions are induced and accelerated through both plasmonic photoinduced catalysis and photothermal effects. The overall contribution of the photothermal effect is found to be related to the incident laser power, the plasmonic wavelength, the separating layer between Au NRs core and Pd NPs, the environmental temperature, and the size of the hybrid nanostructures.

Formic acid has been widely used as the liquid hydrogen storage medium due to its capability of releasing H_2 via the catalytic dehydrogenation. Nevertheless, the activity and selectivity of formic acid dehydrogenation are not satisfied under low temperature. Majima and co-workers have developed Pd-tipped Au NRs (Fig. 10d) and Pd-covered Au NRs (Fig. 10e) hybrids [182], which can work as light absorber and catalytically active site simultaneously, and exhibit efficient plasmon-enhanced catalytic formic acid dehydrogenation under low temperature (5 °C). Fig. 10f shows that with light irradiation, the H_2 evolution rate over Pd-tipped Au NRs increases nearly 15 times compared with that under the dark (conventional thermal catalysis), which is even comparable with that of the conventional thermal catalysis (in dark) at 40 °C using the same catalyst. In addition, the Pd-tipped Au NRs show much higher activity compared to the Pd-covered sample under the same conditions. Finite difference time domain (FDTD) simulation results show that the enhancement of electric field occurs at the tips of the NRs for both of the samples, regardless of the polarization direction (Fig. 10g). Single-particle photoluminescence (PL) spectroscopy discloses that the L-SPR PL intensity dramatically decreases compared to Au NRs, while the T-SPR PL intensity is similar for both samples, indicating that PL at the L-SPR region is quenched by the Pd segment due to the HET and PRET from Au NRs to Pd. These findings may provide a route to improve the atom utilization efficiency of Pd species by selective depositing it only at the field-enhanced sites.

The above discussions show that both HET and the photothermal effects will be generated by plasmonic Au NRs during the SPR decay and provide driving forces to catalytic reactions. However, the two plasmonic effects are unfortunately entangled, making their individual roles still under debate. Xiong et al. have reported that in a model system of bimetallic Au-Pd core@shell nanostructures, the two effects can be disentangled through tailoring the shell thickness at atomic-level precision [59]. To distinctly differentiate photothermal effect from HET, they adopted the well-studied hydrogenation of styrene as a model reaction to assess the plasmonic catalysis performance, considering that plasmonic hot electrons have been recognized to be detrimental to styrene hydrogenation [183]. Fig. 10h shows the performance of styrene hydrogenation using Au NRs-Pd core@shell nanostructures with varied Pd shell thicknesses from 2 layers to 27 layers under different illumination conditions. Without thermostatic control, the yield of ethylbenzene exhibits a volcano shaped relationship with the Pd thickness. Eliminating the photothermal contribution (i.e., with the thermostatic control) can reduce the efficiency down below the control value in the dark due to the detrimental effect from plasmonic hot electrons. Both local heating and hot electron transfer have a nontrivial dependence on Pd shell thickness and irradiation wavelength. The discoveries in this work suggest that the photothermal and HET effects can be separately manipulated through delicate materials design and reaction condition control.

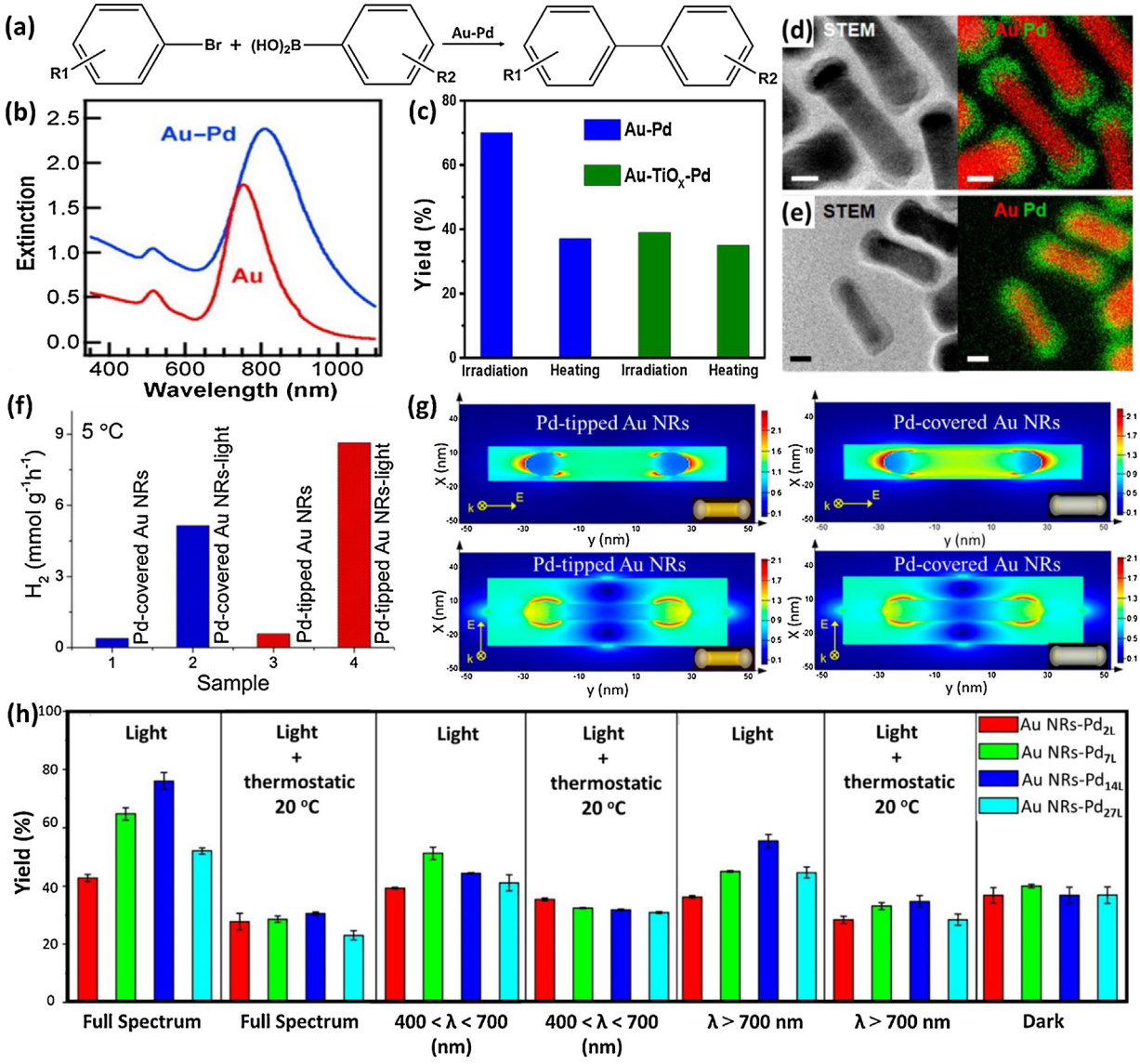

Fig. 10. (a) Schematic of photocatalytic Suzuki coupling reactions with Au-Pd nanostructures. (b) Extinction spectrum of the Au and Au-Pd. (c) Yield of the Suzuki coupling reaction between bromobenzene and m-tolylboronic acid in the presence of Au-Pd or Au-TiOx-Pd under different reaction conditions. (d and e) Scanning TEM (left) and energy dispersive spectroscopy (right) analysis of (d) Pd-tipped Au NRs and (e) Pd-covered Au NRs. (f) The rate of H_2 evolution from formic acid suspensions of different Pd modified-Au NRs under the dark and visible light irradiation (λ > 460 nm, 100 mW cm^{-2}) at 5 °C. (g) Spatial distribution of the SPR-induced enhancement of electric field intensity from FDTD simulation for Pd-tipped Au NRs (left) and Pd-covered Au NRs (right). Here E denotes the vector of the electric field and k denotes the wavevector. (h) Catalytic performance of various Au NRs-Pd core@shell nanostructures in styrene hydrogenation under different reaction conditions. (b and c) Reprinted with permission from [137]. Copyright 2013, American Chemical Society. (d–g) Reprinted with permission from [182]. Copyright 2014, American Chemical Society. (h) Reprinted with permission from [59]. Copyright 2016, American Chemical Society.

The photothermal effect of Au NRs-MOF [58,104,184] and Au NRs-semiconductor [63,116,117,185] composites have also been demonstrated. It is worth noting that the present works on photothermal catalysis of Au NRs-based composites are usually accompanied by the HET process, which results in the complicated charge and energy transfer in the reaction system. A clear scenario of how the geometry (e.g., size and shape) and compositions of Au NRs-based hybrids affect the photothermal catalysis performance is still lacking, and a delicate reaction system design to eliminating the HET contribution is highly sought after. Toward this end, monochromatic light sources with variable wavelength and intensity could be employed to unravel the SPR effects and determine their relative contributions on the catalysis activity [186–188]. In addition, the geometrical configuration of plasmonic Au NRs-based composites should be taken into account to verify the different SPR effects. The HET effect requires intimate contact at the interface between the two functional components. Control experiments using an insulating interlayer with variable thicknesses at the interface can help in banishing the HET effect [55,64].

Process-intensified engineering strategies for efficient photoredox catalysis

Since multiple physicochemical steps are involved in the photoredox catalysis reactions [2,189], the performance of Au NRs-based composites can be enhanced by diverse optimization approaches. In this section, the strategies employed to maximize solar energy conversion efficiency of Au NRs-based composites will be categorized and discussed in four sub-sections (Fig. 11a): 1) enhancing light absorption by plasmonic units design, 2) promoting charge carriers separation and transfer by heterointerface engi-

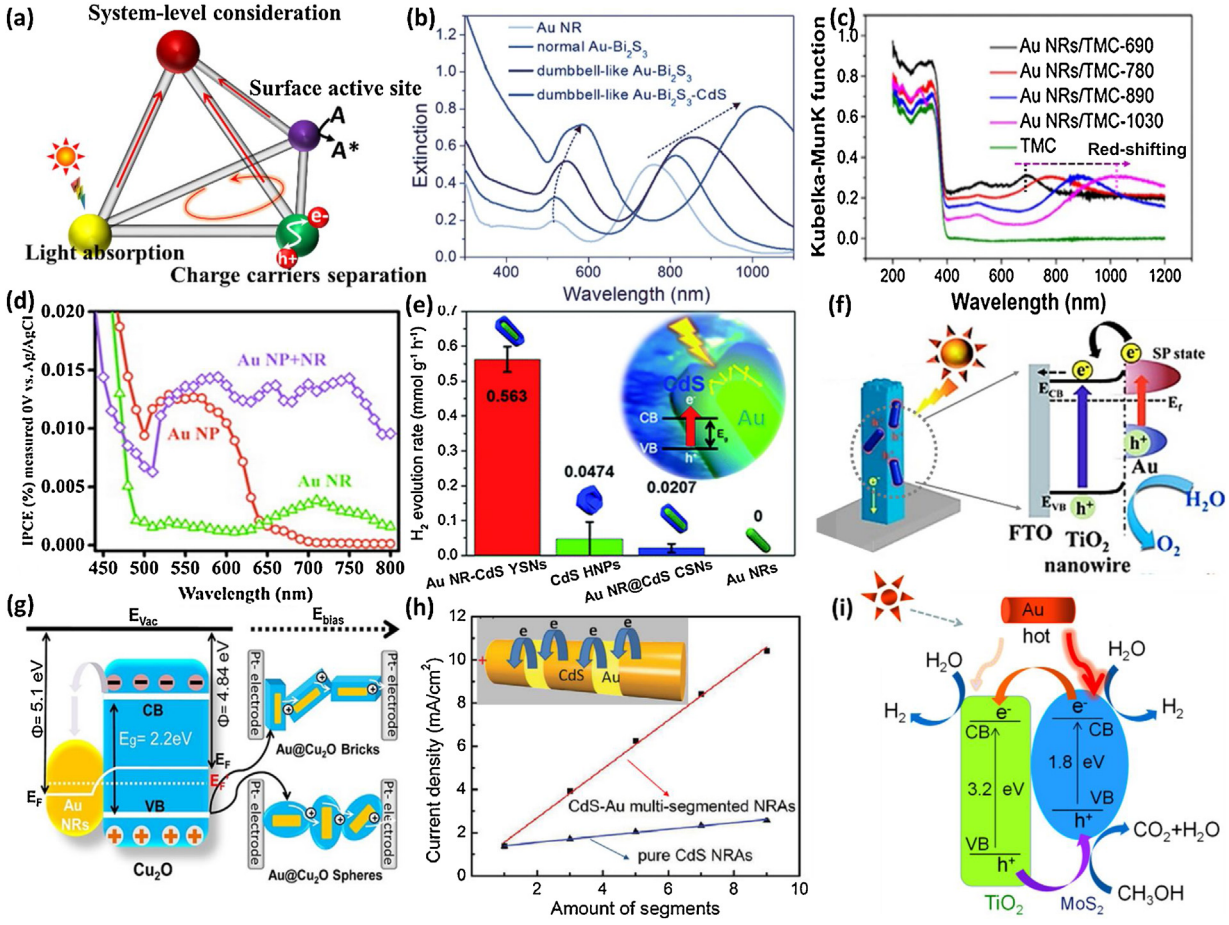

Fig. 11. (a) Schematic description of process-intensified engineering strategies for efficient photoredox catalysis. (b) Extinction spectra of different Au NRs-based core@shell hybrid structures and initial Au NRs. (c) UV–vis diffuse reflectance spectra of blank TiO_2 mesocrystals (TMC) and Au NRs/TMC with different aspect ratios. (d) IPCE plots of different Au-decorated TiO_2 electrodes in the incident wavelength between 450 and 900 nm. (e) H_2 evolution rates over Au NR-CdS YSNs, Au NR-CdS CSNs, CdS HNPs and Au NRs samples. The inset shows the schematic illustration of the synergism between the radiative relaxation of the plasmon energy of the Au NRs yolks and the multiple reflections of the incident light within the voids due to the yolk/shell structure. (f) Schematic illustration of charge carrier transfer in Au NRs-decorated TiO_2 electrode. (g) Schematic illustration of charge carrier transfer and arrangement of particles between electrodes in Au@Cu_2O system. (h) The linear relationship between the photocurrent intensities and the amount of segments in the multi-segmented CdS-Au nanorod arrays (NRAs) and the pure CdS NRAs photoanodes. The inset shows the schematic diagram of charge carrier transfer in multi-segmented CdS-Au NR. (i) Schematic illustration of energy band structure and electron-hole separation of (MoS_2-TiO_2)/Au substrate. (b) Reprinted with permission from [194]. Copyright 2015, Wiley. (c) Reprinted with permission from [193]. Copyright 2017, Elsevier. (d and f) Reprinted with permission from [149]. Copyright 2013, American Chemical Society. (e) Reprinted with permission from [109]. Copyright 2018, Royal Society of Chemistry. (g) Reprinted with permission from [197]. Copyright 2014, American Chemical Society. (h) Reprinted with permission from [198]. Copyright 2014, Wiley. (i) Reprinted with permission from [199]. Copyright 2017, Nature Publishing Group.

neering, 3) enriching surface active site by co-catalyst strategies, and 4) design and optimization from a system-level consideration.

Enhancing light absorption by photoabsorption units design

As the first step of the photoredox catalysis process, the light absorption ability of photocatalysts directly determines the generation density of charge carriers and subsequently influences the overall solar energy conversion efficiency [11,190]. Unfortunately, many reactive photocatalysts usually have wide bandgap, and thus can utilize only short-wavelength UV–vis light, which accounts for less than 50% of the total energy from the sun (solar light consists of 5% UV, 43% visible and 52% IR light) [9,191]. Hence, from the viewpoint of solar energy harvesting, extending the light absorption range of the photocatalysts to the Vis-NIR region is essential to enhance the solar-to-chemical energy conversion efficiency [192,193]. A prominent advantage of Au NRs is that the L-SPR can be easily tuned in NIR region by adjusting their shape and size. Moreover, the T-SPR band of Au NRs located in the visible region is stable and excellently matches the peak wavelength of solar irradiation spectrum. However, in extinction spectra, the intensity of T-SPR is only 20–40% of L-SPR, which indicates that the harvesting of visible light energy is limited for Au NRs.

Wang's group has reported a facile method to manipulate the SPR absorption of Au NRs-based core@shell hybrid structures [194]. Accompanying with the coating of metal sulfides (including CdS, Bi_2S_3, ZnS and Cu_xS), the morphology of Au NRs synchronously transforms to the dumbbell-like shape. Due to the reconstruction of Au NRs core and the deposition of sulfide shell, the T-SPR of Au NRs is highly enhanced. As shown in Fig. 11b, the initial Au NRs exhibit two extinction bands at 514 and 780 nm, corresponding to the T-SPR and L-SPR, respectively. After the Bi_2S_3 layers are coated, the L-SPR band red-shifts to 810 nm with the slight T-SPR red-shifting to 519 nm because of the increased refractive index of the surrounding medium. The intensity ratio of T-SPR to L-SPR ($R = I_{T\text{-}SPR} / I_{L\text{-}SPR}$) changes little (from 0.4 to 0.3). As for the dumbbell-like Au-Bi_2S_3 NRs, the T-SPR is red-shifted to 546 nm and the L-SPR is red-shifted to 860 nm. Both the intensities of T-SPR and L-SPR are enhanced and the R is increased to 0.8. It implies that the SPR absorption for the dumbbell-like Au-Bi_2S_3 core@shell NRs is greatly enhanced, especially for the T-SPR band, which is about 3 times as that of the initial Au NRs. Owing to the highly ascendant visible light absorption and

strong LEF, the photocatalytic activity of dumbbell-like Au-Bi_2S_3 NRs is largely boosted compared with pure Bi_2S_3 and normal Au-Bi_2S_3 NRs by testing the photodegradation rate of Rhodamine B (RhB). Moreover, the second-layer CdS semiconductor, which has a bandgap perfectly matched with the solar irradiation as well as the T-SPR of Au NRs, can be coated on Au-Bi_2S_3 NRs and double-shell Au-Bi_2S_3-CdS heterostructures show further improved visible light absorption and photoactivity.

Another important factor affecting the overall light harvesting efficiency of Au NRs-based hybrids is the shape of plasmonic Au NRs. Majima and co-workers have demonstrated that Au NRs with controllable size and tunable SPR absorption loaded onto anatase TiO_2 mesocrystals can achieve the broad-band light harvesting [193]. The aspect ratio of Au NRs has great impacts on the photocatalytic activity for H_2 production of the composites. On one hand, the higher aspect ratio is beneficial for the NIR light harvesting and improves the photoactivity. On the other hand, as increase of aspect ratio, the L-SPR absorption peak shifts toward longer-wavelength region with lower photon energy (Fig. 11c), resulting in the low efficiency of HET. Thus, the optimal activity is achieved over the composites with a medium aspect ratio of Au NRs (about 3.2). Gong et al. have reported that the Au NRs-TiO_2 yolk/shell photocatalysts with different aspect ratios of Au NRs core exhibit significantly different photocatalytic performance for BA oxidation [112]. The optimal photoactivity was obtained over the sample with Au NRs aspect ratios of 2.4, due to its efficient Vis-NIR light harvesting. These works highlight that the hot carrier generation efficiency is directly influenced by the shape of Au NRs.

The Au NRs-based composites with improved light harvesting can also be accomplished by integrating different plasmonic units in one ensemble. For example, it has been found that the photoactivity of Au-decorated TiO_2 electrodes for PEC water oxidation can be effectively tuned in the Vis-NIR region by manipulating the shape of the decorated Au nanostructures [149]. The IPCE (Fig. 11d) results reveal that the Au NPs decorated TiO_2 electrodes exhibit significantly enhanced photoactivity in visible (λ = 450–650 nm) region. For Au NRs decorated TiO_2 electrodes, the photoactivity enhancement is, however, observed in the NIR region (λ = 650–900 nm) only. Significantly, the TiO_2 electrodes deposited with a mixture of Au NPs and Au NRs show enhanced photoactivity in the entire Vis-NIR region due to the increased optical absorption of TiO_2 associated with SPR electrical field amplification.

In addition to manipulating the photoabsorption of the plasmonic components, optimizing the geometrical arrangement and dielectric environment of the building units have demonstrated to be another effective strategy to enhance the optical absorption of the Au NRs-based composites. Tachikawa et al. have reported that Pt-modified Au NRs can be used for producing H_2 under Vis-NIR light irradiation [135]. The Pt-tipped sample exhibits much higher L-SPR intensity and photoactivity compared with Pt fully covered sample. The obvious decrease in L-SPR intensity of Pt-covered sample is ascribed to the complete encapsulation of Au NR core by the Pt shell, which possesses distinct plasmon damping effect. A novel heterostructure composed of Au NRs yolk and CdS semiconductor shell has recently been developed by Han's group [109]. The Au NRs-CdS yolk/shell nanostructures (Au NR-CdS YSNs) exhibit superior photocatalytic H_2 evolution performance under visible light irradiation over their core@shell nanostructured (Au NR-CdS CSNs) counterparts, CdS hollow nanoparticles (CdS HNPs), and Au NRs (Fig. 11e). A series of mechanistic studies on the photocatalysis corroborate that the photoactivity enhancement of the yolk/shell nanostructures is due to the synergism between the multiple reflections of the incident light within their voids provided by the yolk/shell structure and the radiative relaxation of the plasmon energy of the Au NRs yolks, which promote the light absorption of CdS that can drive the photocatalysis (inset of Fig. 11e).

Taken together, the light harvesting efficiency of Au NRs-based composites is dependent on the shape, size and components of the plasmonic units as well as the geometrical arrangement and dielectric environment of the building units. Maximizing the energy transfer from photons to photoactive components requires the rational understanding of structural design principle [4,7], because randomly hybridizing counterparts would often shield the SPR intensity and LEF of plasmonic Au NRs or weaken the net photoabsorption of semiconductors [22,51,135,195].

Promoting charge carrier separation and transfer by heterointerface engineering

Fast charge carriers recombination is the main limiting factor on the substantial performance improvement of the most photoredox catalysis systems [5,155]. Therefore, not only the high generation density of charge carriers should be satisfied, but also these electrons and holes should be efficiently coupled into transport medium before they get recombined [5]. Toward this end, tremendous efforts have been devoted to exploring multifarious strategies to harness the plasmonic effects and co-catalyst functionality of Au NRs by maximizing the interfacial charge carrier transfer efficiency, which has proven to be effective to enhance the photoactivity. In general, the charge carrier separation and transfer efficiency depend on the interfacial contact, overall morphology, component arrangement and band alignment of the composite materials.

Considering that the photogenerated charge carrier transfer predominantly occurs across the interfacial domain in Au NRs-based composite systems, maximizing interfacial contact between Au NRs and other components is significant on the reduction of these charge carrier recombination. However, some organic ligands are always required in colloidal synthesis for stabilizing Au NRs [23], which often still remain at the heterointerface and thus form an insulating layer that prevents the formation of effective interfacial contact. To solve this problem, a delicately designed surfactant removal method has been developed, which is based on a $HClO_4$ oxidative process [135,139]. Benefiting from this effective strategy, the obtained photocatalysts show superior activity to the sample without the oxidative treatment. In addition, ligand-exchange method has been usually utilized to enhance the interfacial contact [141,149,196]. Au NRs-decorated TiO_2 nanowire arrays prepared by ligand-exchange with MPA show efficient hot electron transfer from Au to TiO_2 semiconductor through the interface (Fig. 11f) [149]. The interfacial charge carrier transfer efficiency is also dependent on the overall morphology of the composites. Yu et al. have demonstrated that tuning the morphology of Au@Cu_2O core@shell NPs from brick to spherical shape can facilitate the charge flow and significantly decrease the charge carrier transfer resistance, which is due to the presence of sharp edges in brick like structure hindering the close contact between the particles (Fig. 11g) [197].

Although combination of Au NRs with semiconductors shows a significant promise to prevent the recombination of electron-hole pairs in Au NRs or semiconductors, incorporating an overly large amount of Au NRs may lead to the undesired defects and resultant recombination of photogenerated charge carriers [38,169]. To balance these two effects, controllable arrangement of the ordered Schottky barriers in the composite photocatalysts is necessary. Chen and co-workers have reported the fabrication of programmable photoanode based on multi-segmented CdS-Au nanorod arrays (NRAs) and demonstrated its high efficiency and programmability in PEC catalysis [198]. As disclosed in Fig. 11h, the photoactivity of CdS-Au NRAs is greatly enhanced compared to pure CdS NRAs with that same length. Moreover, the activity of the NRAs shows programmable photocatalysis behavior and can be linearly increased by increasing the number of segments in the composites,

which indicates that the photogenerated electrons can easily flow across the series of height-reduced Schottky barriers when positive bias is applied at the photoanode (inset of Fig. 11h). Higher photocatalytic activity could be achieved by further increasing the number of segments.

Rational designing and optimizing the electron transfer paths can also benefit the improvement of charge carrier transfer efficiency. In this direction, constructing multi-component hybrids with multiple heterointerface has been explored. Ternary (MoS_2-TiO_2)/Au hybrid has been fabricated by loading plasmonic Au NRs on the MoS_2 NSs coated TiO_2 NRs arrays and used as PEC cell for H_2 generation [199]. The highest photocurrent and photoactivity are obtained over the (MoS_2-TiO_2)/Au sample, which is benefited from the plasmon-coupled multichannel electron transfer (Fig. 11i). In detail, the Au NRs have intense SPR absorption and work as the photosensitizers to produce hot electrons. The hot electrons can get over the Schottky barrier and inject into the CB of MoS_2 and TiO_2. In addition, the band alignment between MoS_2 and TiO_2 is favorable for the electron transfer from the CB of MoS_2 to the CB of TiO_2 and suppresses the photogenerated carrier recombination. Moreover, the inserted MoS_2 NSs connect neighboring TiO_2 NRs and act as the bridge routes, which further promote the electron transfer along the TiO_2 channel to the conductive substrate.

Enriching surface active site by co-catalyst strategies

Another bottleneck for efficient photoredox catalysis is the low activation ability of semiconductor surfaces [191,200]. Once the charge carriers are generated and injected into the semiconductors, they should be timely consumed by redox reactions on their surface. However, the semiconductor surface often does not offer highly active sites to activate the chemical bonds in many molecules and decrease the overpotential for the reactions such as the H_2 and O_2 evolution, thereby limiting the catalytic activity of photocatalysts [191]. The combination of co-catalysts with semiconductors has been widely used to resolve this problem, because the co-catalysts can accept the electrons or holes from the semiconductors, tune charge carriers kinetics, and act as the alternative highly active sites for redox reactions. Nanostructured Pd and Pt have been demonstrated to be the potential co-catalysts for many reactions owing to their strong affinity interaction with organic molecules and extremely low overpotential for proton reduction [112,138,184,201–203], which can be employed to overcome the sluggish kinetics of the reactions.

Tang and co-workers have demonstrated that the photoactivity of Au NRs for molecular oxygen activation and carbon-carbon coupling reactions can be significantly enhanced by constructing Au NRs@Pd superstructures (Au@Pd SSs), where the ordered Pd nanoarrays are precisely grown on Au NRs surfaces (Fig. 12a) [22]. Taking molecular oxygen activation reaction as an example (Fig. 12b), bare Au NRs show no discernible photoactivity under both light irradiation and dark conditions, in spite of its significant electric field enhancement and hot electron generation efficiency (Fig. 12c). The noticeable photoactivity of Pd NPs and the mixture of Au NRs and Pd NPs keeps unchanged with respect to that under dark environment. These results suggest that the oxygen activation occurs on active Pd sites. The photoactivity enhancement of Au NRs@Pd is closely related to the organization of Pd NPs on the surface of Au NRs. The Au@Pd SSs show higher activity than the samples of Au@Pd NDs with Pd NPs randomly attached on the surfaces of Au NRs and Au@Pd CSs with continuous Pd thin shells coating on Au NRs. Since the composition weight, absorption band and reaction temperature of these Au@Pd nanostructures are controlled to be the same, such prominent plasmon enhancement property of Au@Pd SSs in oxygen activation and carbon-carbon coupling reaction should be attributed to their structure superiority, where the ordered open structure of Pd nanoarrays on-rod exposes rich active sites for incoming reactants.

On the basis of a semiconductor-like MOF (i.e., MIL-125), the composites integrated SPR excitation of Au NRs and nonplasmonic Pt NPs co-catalyst into MIL-125 have recently been reported by Jiang's group [184]. To build the heterojunctions, Pt NPs are firstly dispersed into or supported on MIL-125 to afford Pt@MIL-125 and Pt/MIL-125, respectively. Subsequently, Au NRs are assembled onto Pt@MIL-125, Pt/MIL-125 and pure MIL-125, respectively, to produce Pt@MIL-125/Au, Pt/MIL-125/Au and MIL-125/Au (Fig. 12d). In the composites, the interface between the MIL-125 and Au NRs allows the plasmonic hot electrons injecting from SPR-excited Au into the lowest unoccupied molecular orbital (LUMO) of the MOF. The nonplasmonic Pt/MOF interface is to establish a Schottky barrier as the charge "pump", which steers the charge flow and allows the electrons delivery to specific sites for further proton reduction (inset of Fig. 12e). As a result, the Pt@MIL-125/Au presents an exceptionally high photocatalytic H_2 production rate by water splitting under visible light irradiation, far superior to MIL-125/Au and other counterparts with similar Pt or Au contents (Fig. 12e). Moreover, thanks to the more effective spatial separation of Pt and Au, the Pt@MIL-125/Au presents much better charge separation efficiency and photoactivity than Pt/MIL-125/Au. This work highlights the synergetic effect of coupling co-catalyst strategies with the formation of charge flow toward efficient photocatalytic H_2 production.

Nonprecious metal co-catalysts, such layered MoS_2, have also been demonstrated to be the promising hydrogen evolution reaction (HER) catalysts due to the optimal affinity of H_2 on the unsaturated sulfur atoms on the edges of MoS_2 NSs [204]. It has been reported that MoS_2 hybridized with Au NRs can improve the HER activity of Au NRs and MoS_2 [74,147,148]. Xia et al. have synthesized Au NRs/MoS_2 NSs hybrids (Au-MoS_2) for plasmon-activated HER [74]. In this system, Au NRs acting as the light absorbers generate electron-hole pairs during SPR excitation, and MoS_2 NSs working as the active sites and electron acceptors facilitate HER. As shown in Fig. 12f, in contrast to blank Au NRs and MoS_2, the plasmonic Au-MoS_2 hybrids dramatically improve the HER performance and decrease the onset potential for H_2 evolution under L-SPR excitation of Au NRs.

Spatially separated dual co-catalysts modified Au NRs-based hybrid structure, which are composed of Au NRs with Pt modified crystalline TiO_2 layer on its top and Co-based OEC on its bottom side (Fig. 12g), has been demonstrated by Moskovits et al. [205]. All charge carriers involved in the water oxidation and reduction steps on this type of hybrid nanostructures are found to be originated from the SPR excitation of Au NRs. The excited plasmons of Au NRs decay into electron-hole pairs. The hot electrons transport to the Au/TiO_2 interface and overcome the Schottky barrier to enter in the CB of TiO_2, and finally reach the surface Pt active site to reduce H^+ (Fig. 12h). On the other hand, the holes transport to the Co-based OEC to produce O_2. Fig. 12i shows the amounts of both O_2 and H_2 produced under full solar illumination (AM 1.5, 300 mW cm^{-2}) over a 6 h period. The rate of H_2 production are 2.8 mmol h^{-1} g^{-1} under full solar irradiation without any hole scavenger. Although the rates of H_2 and O_2 production on this type of nanostructures are not high, the use of electron-hole pairs derived from the SPR photoexcitation of Au NRs in overall water splitting has been unambiguously demonstrated. This work reveals a new paradigm for designing plasmonic catalysts with spatially separated dual co-catalysts loading for overall water splitting.

Design and optimization from a system-level consideration

With the key advances in the literatures, the above three strategies have been proven to be efficient for better utilization of the

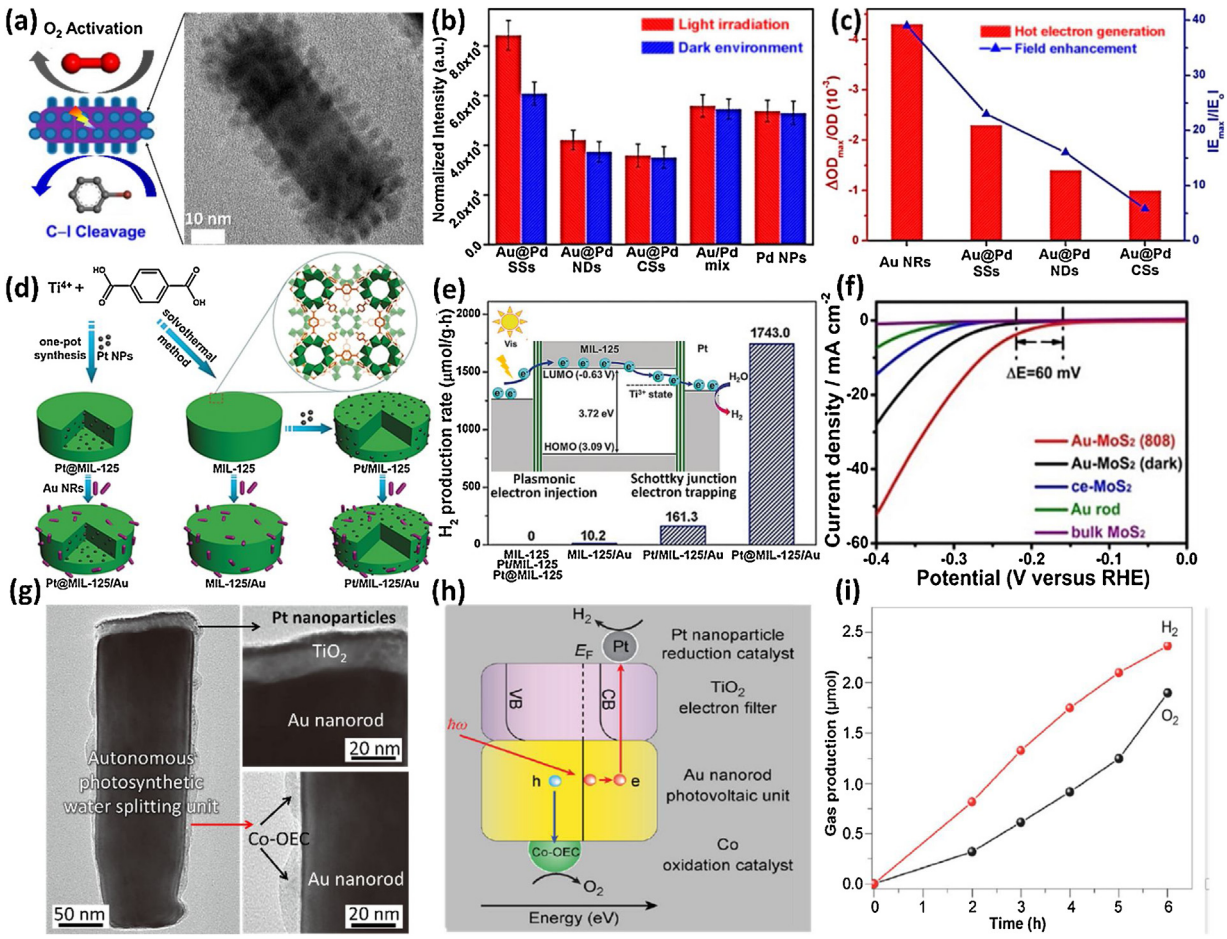

Fig. 12. (a) Schematic description of photoredox catalysis over Au@Pd SSs for molecular oxygen activation and carbon-carbon coupling reactions. The right panel show the TEM image of Au@Pd SSs. (b) Normalized singlet oxygen signal intensity of varied nanostructures under both dark environment and light irradiation. (c) Correlation between hot electron generation efficiency and field enhancement among different Au NR-based nanostructures. (d) Schematic illustration showing the synthesis of Pt@MIL-125/Au and the corresponding Pt/MIL-125/Au and MIL-125/Au analogues. (e) Photocatalytic H_2 production rates of different catalysts. The inset shows the electron migration at the two metal-MOF interfaces based on the energy levels. (f) HER polarization curves obtained on different catalysts. (g) TEM image (left) of the photosynthetic unit and magnified views of the Pt/TiO_2 cap (top right) and the Co-OEC (bottom right). (h) Energy level diagram superimposed on a schematic of the plasmonic solar water splitter, showing the proposed processes occurring in its various parts and in energy space. (d) Measured O_2 and H_2 productions as a function of irradiation time under full solar illumination (AM 1.5, 300 mW cm^{-2}) illumination. (a–c) Reprinted with permission from [22]. Copyright 2017, American Chemical Society. (d and e) Reprinted with permission from [184]. Copyright 2018, Wiley. (f) Reprinted with permission from [74]. Copyright 2015, American Chemical Society. (g–i) Reprinted with permission from [205]. Copyright 2013, Nature Publishing Group.

unique optical, electrical and catalytic properties of Au NRs for specific photoredox reactions. Nevertheless, these strategies often focus on only investigating an isolated process or individual constituents of the photoredox catalysis system. One major point could be learned from the nature photosynthetic organisms is that designing an efficient photoredox catalysis system requires optimizing the entire ensemble from a system-level consideration [206]. In this context, Xu et al. have shown that the finely control of a series of factors, including the shape and loading contents of plasmonic units, interfacial interaction, charge carrier transfer paths and surface active sites in Au NRs-based heterostructures, can result in progressively improved performance for Vis-NIR light-driven plasmonic photocatalysis [138].

In detail, they have firstly demonstrated that coupling Au NRs with semiconductor CdS (Step 1 in Fig. 13a) can dredge the hot electrons generated from the SPR excitation of Au NRs to participate in photocatalysis processes, and strengthening the interfacial interaction (Step 2 in Fig. 13a) by the surface charge tuning enables more efficient extraction and injection of hot electrons from the Au NRs to CdS across the interfacial domain. Subsequently, they have argued that the shape (aspect ratio) and loading contents of Au NRs have great impacts on the photocatalytic performance (Step 3 in Fig. 13a). As mentioned above, high SPR absorption intensity and resonance energy of Au NRs result in more energetic hot electrons that can inject over the Schottky barrier at the semiconductor/metal interface under L-SPR excitation. On one hand, increasing the aspect ratio of Au NRs is beneficial for improving the SPR absorption intensity, but will reduce the resonance photon energy. On the other hand, higher content of Au NRs loading results in higher SPR absorption intensity. However, excess Au NRs loading in the composites can lead to strong photon scattering and charge recombination, thus suppressing the photoactivity. The optimal aspect ratio and loading content of Au NRs in this work are 3.3 and 2 wt.%, respectively.

The above optimization strategies allow higher efficiency of HET from Au NRs into the CB of CdS. However, the overall efficiency of the Au-CdS composites is still limited by the well-known factors, such as fast damping and cooling of hot charge carriers, slow charge migration rate, random charge diffusion directions, and the low activation ability of semiconductor surfaces [191,207,208]. In this context, they have utilized metal (Au, Ag or Pt) NPs as the co-catalysts to construct ternary composites, aiming to modulate the spatial transfer channels of hot charge carriers, and thus further improve the photocatalytic activity of Au-CdS (Step 4 in

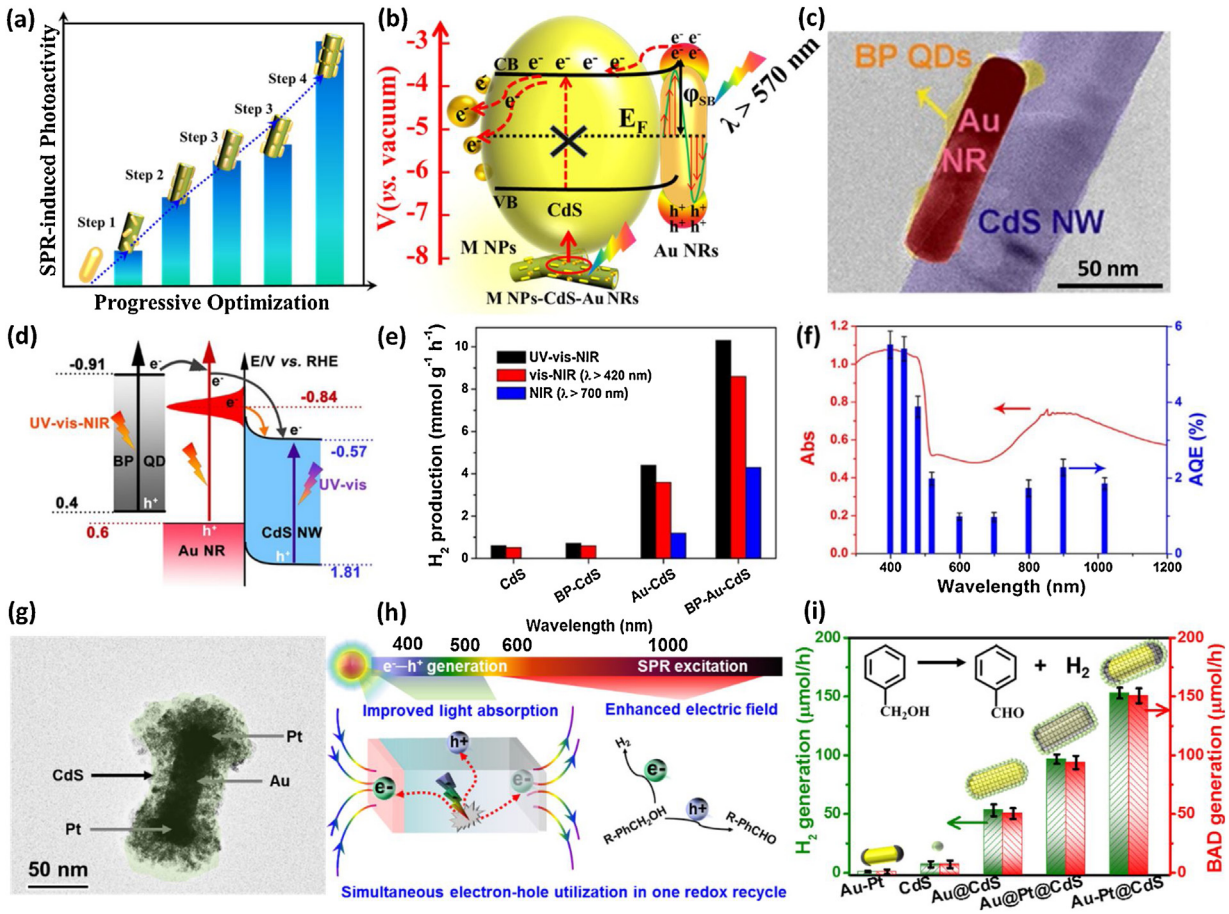

Fig. 13. (a) Schematic illustration of principle on how to make efficient use of the prominent SPR property of Au NRs toward boosting photocatalytic activity. (b) Schematic illustration of the hot charge carrier generation, separation, and transfer in the ternary M NPs-CdS-Au NR composites. (c) TEM image of ternary BP-Au-CdS composite. (d) Schematic illustration of electron-transfer pathway in the BP-Au-CdS system. (e) Comparison of H_2 production rate over different samples under UV–vis-NIR, Vis-NIR, and NIR light irradiation. (f) Diffuse reflectance spectroscopy (left axis, red line) and AQE (right axis, blue column) of BP-Au-CdS. (g) TEM image shows the direct and multiple metal-semiconductor and metal-metal interfacial contact in Au-Pt@CdS. (h) Schematic illustration of the efficient charge carriers generation, transfer and utilization over Au-Pt@CdS photoredox catalysis system. (i) H_2 and BAD generation rate in the photocatalytic conversion of BA under Vis-NIR light (λ > 420 nm) irradiation over Au-Pt, CdS and metal-CdS hybrids. (a and b) Reprinted with permission from [138]. Copyright 2017, Wiley. (c–f) Reprinted with permission from [79]. Copyright 2018, American Chemical Society. (g–i) Reprinted with permission from [212]. Copyright 2019, Royal Society of Chemistry.

Fig. 13a). These step-by-step modulation methodologies finally result in the multiple synergy promotion of separation and transfer of hot charge carriers generated from the SPR excitation of Au NRs, while the CdS and metal NPs respectively act as the mediator and co-catalysts to boost the extraction and transfer of hot charge carriers from Au NRs and provide effective reduction sites, thereby leading to the distinctly enhanced activity toward photoreduction of nitroaromatics and water splitting (Fig. 13b).

In another work based on Au-CdS composites, Zhang et al. have reported that Au NRs serve as both electron relays and plasmonic electron donors in a ternary heterostructure (BP-Au-CdS), consisting of black phosphorus (BP) quantum dots (QDs), CdS NWs and Au NRs [79], which can synergistically utilize the SPR enhancement mechanism of Au NRs, photosensitizing effect of QDs and bandgap photoexcitation of semiconductors for efficient H_2 generation under full solar spectrum irradiation. Fig. 13c shows the TEM image of ternary BP-Au-CdS composites, which indicates that BP QDs are deposited directly on the surface of Au NRs, while Au NRs are decorated along the side of CdS NWs to form 1D-1D interfacial interaction. The first principles calculations suggest that a Schottky barrier can be formed between the Au (100) surface and CdS (100) surface, and an Ohmic contact is formed in the case of Au and BP. Thus, the structure arrangement in Fig. 13c is very essential for prolonging the lifetime of charge carriers photogenerated from both BP QD and Au NRs due to the steered charge flow, as disclosed in Fig. 13d.

The H_2 production rates of BP-Au-CdS have been examined under different illumination conditions, including full solar spectrum (UV–vis-NIR) light, Vis-NIR (λ > 420 nm) light and NIR (λ > 700 nm) light irradiation. As shown in Fig. 13e, compared with binary counterparts, the ternary BP-Au-CdS composites exhibit the highest photoactivity under similar conditions. Notably, when the irradiation source turns to NIR light illumination, the photocatalytic H_2 evolution rate of BP-Au-CdS can still reach 4.3 mmol g^{-1} h^{-1}. The wavelength-dependent apparent quantum efficiency (AQE) of H_2 production over BP-Au-CdS shows that the action spectrum of the AQE is basically in agreement with the absorption spectrum, further confirming the full solar spectrum-responsive photocatalytic H_2 production. The BP-Au-CdS hybrids present several superiorities as follow: (1) BP QDs exhibit unique optical properties due to quantum confinement and edge effects, meanwhile the broadened bandgap and up-shifted CB edge endow the photogenerated electrons in BP QDs with improved reduction activity. (2) Au NRs serve as the electron relays to dredge the charge transfer channels between BP and CdS, while the intimated interfacial contact between Au NRs and CdS enables the effective electron delivery from Au to CdS. (3) Au NRs with visible and NIR plasmonic absorption offer hot electrons to CdS, further contributing to the photocatalytic performance. These

findings would promote the development of full solar spectrum-responsive Au NRs-based heterostructure photocatalysts with high performance.

To achieve efficient solar-to-chemical energy conversion, both the photogenerated electrons and holes should be synchronously utilized without sacrificial agent consumption [209–211]. Toward this end, Xu's group has recently reported a controllable design of bimetal-semiconductor hybrids for simultaneous H_2 and value-added aldehyde production from one redox cycle [212]. Specifically, taking advantage of Au NRs, Pt NPs, and CdS as plasmonic metal, nonplasmonic co-catalyst and semiconductor respectively, they have constructed a CdS deposited anisotropic Pt-tipped Au NRs (Au-Pt@CdS) hybrid, which features the multiple metal-semiconductor and metal-metal heterointerface (Fig. 13g). They have demonstrated that integrating co-catalytic factor with semiconductor photoexcitation and SPR resonance modes in different optical response region by rational assembly of Pt NPs and CdS on the surface of Au NRs can provide the spatial transfer multichannel for electrons and boost the local electric field, promoting the generation and migration of electron-hole charge carriers (Fig. 13h). As a result, the Au-Pt@CdS exhibits distinctly higher photoactivity than blank CdS and other metal-CdS hybrids counterparts for photocatalytic conversion of alcohol to aldehyde and H_2 by simultaneous utilization of photogenerated holes and electrons (Fig. 13i). This work could be instructive for further rational design of plasmonic bimetal- or multimetal-semiconductor dual-function photocatalytic reaction system toward efficient redox catalysis.

Concluding remarks and future perspectives

In summary, we have provided a detailed review of the structure, plasmonic properties, as well as the synthetic chemistry of Au NRs-based hybrid materials with tailored architectures. The latest progresses on utilizing Au NRs-based hybrids for different photoredox catalysis applications, and particularly the various process-intensified engineering strategies for enhancing the performance of hybrid materials have been highlighted. Clearly, the utilization of Au NRs has attracted particular attention for the development of SPR-mediated photoredox catalysis due to the fact that the introduction of Au NRs into solar-to-chemical energy conversion can efficiently improve the performance by harnessing their highly focused electric field, effective photothermal conversion, unique hot electron generation and remarkable co-catalytic effect. From our perspective, several challenges need to be overcome for further advancing this research topic.

First, although a large fraction of studies have been devoted to the preparation of Au NRs-based hybrid nanostructures, the morphology and heterointerface of the overall nanostructures have not been controlled very well owing to the distinct differences in the bonding nature and crystalline structure among the different functional components. For most of the hybrid structures obtained from ex-situ synthesis procedure, the interfacial contact is usually not very tight. Some organic molecules have been utilized to modify the surface of Au NRs or second component for enhancing the interfacial interaction. However, these molecules are often not conductive and may be decomposed during the catalytic reactions, which ultimately affect the charge carrier transfer and activity of the hybrids. Additionally, for the nanostructures that are prepared by in-situ approach, the morphology, position, size, and crystallinity of the subsequently formed second component are often difficult to control. But these parameters play a crucial influence on the properties and performance of the hybrids, as discussed in the early parts of this review. Therefore, a simple yet efficient method to produce Au NRs-based hybrid structures with better control of the size and shape of the overall nanostructure, as well as the individual components and heterointerface is highly sought after.

Second, despite efforts paid to illustrate the working mechanism of Au NRs-mediated photoredox catalysis, the activity enhancement mechanism still needs further in-depth investigation. For example, in most reaction systems, the photothermal conversion, hot electrons transfer and enhanced electric field effects are simultaneously involved, which results in an obstacle to accurately depicting the function of each effect. The apparent activation barrier for photothermal catalysis could be decreased by SPR-induced thermal effect [213,214]. But a viable experimental approach for directly probing the SPR-induced local temperature within the nanometer size regime is still scanty. In these regards, developing advanced detection technology to dynamically monitor the local surface temperature of plasmonic units, and delicately designing the reaction systems to quantify the contributions of each effect in targeted catalysis are desirable.

Third, the application scope of Au NRs-based photoredox catalysis could be extended to various reactions in addition to photocatalytic non-selective pollutants degradation and water splitting. Some emerging fields, such as CO_2 reduction, N_2 fixation and selective biomass transformation, need to be paid more attention. Recent works show that some molecules can be excited from a low-energy state to a high-energy state by the incident photons, and these reactant molecules in excited states can interact with SPR-excited metal nanostructures to elongate bond lengths and lower reaction barriers [213,215–217]. The generation of energetic hot charge carriers, enhanced electric field and spatially heterogeneous hotspots from plasmonic Au NRs-based materials may thus offer great opportunities for producing unique excited states, tailoring the catalytic reaction pathways and even selectively cleaving chemical bonds [218]. Therefore, there are wide promising opportunities toward these inspiriting directions.

Last, developing theoretical analytical models, that can rigorously describe the plasmon coupling phenomenon and electron transfer process among Au NRs, functional components and reactant or product molecule, is very important to identify the optimal geometry and composition of Au NRs-based plasmonic catalysts for the targeted photoredox reactions. Joint efforts of experiment and theory are expected to provide reliable analyses of the excited states, the reaction pathways, the distribution of electric field and the exact energy levels of energetic charge carriers. Looking to the future, we believe that devotion of great efforts to these directions would generate exciting new scientific development and advance technological applications in this exciting field.

Acknowledgments

The support from the National Natural Science Foundation of China (NSFC) (21872029, U1463204, U1463205, 21173045), the Award Program for Minjiang Scholar Professorship, the Natural Science Foundation (NSF) of Fujian Province for Distinguished Young Investigator Rolling Grant (2017J07002), the Independent Research Project of State Key Laboratory of Photocatalysis on Energy and Environment (NO. 2014A05), and the 1st Program of Fujian Province for Top Creative Young Talents is gratefully acknowledged.

References

[1] J.C. Colmenares, R. Luque, Chem. Soc. Rev. 43 (2014) 765–778.
[2] M.-Q. Yang, N. Zhang, M. Pagliaro, Y.-J. Xu, Chem. Soc. Rev. 43 (2014) 8240–8254.
[3] K.-Q. Lu, X. Xin, N. Zhang, Z.-R. Tang, Y.-J. Xu, J. Mater. Chem. A 6 (2018) 4590–4604.
[4] S.-H. Li, N. Zhang, X. Xie, R. Luque, Y.-J. Xu, Angew. Chem. Int. Ed. 57 (2018) 13082–13085.

[5] N. Zhang, M.-Q. Yang, S. Liu, Y. Sun, Y.-J. Xu, Chem. Rev. 115 (2015) 10307–10377.
[6] B. Weng, K.-Q. Lu, Z. Tang, H.M. Chen, Y.-J. Xu, Nature Commun. 9 (2018) 1543.
[7] R. Long, Y. Li, L. Song, Y.J. Xiong, Small 11 (2015) 3873–3889.
[8] P. Zhang, T. Wang, J. Gong, Adv. Mater. 27 (2015) 5328–5342.
[9] L. Yuan, S.-F. Hung, Z.-R. Tang, H.M. Chen, Y. Xiong, Y.-J. Xu, ACS Catal. 9 (2019) 4824–4833.
[10] B. Weng, M.-Y. Qi, C. Han, Z.-R. Tang, Y.-J. Xu, ACS Catal. 9 (2019) 467–4642.
[11] C. Han, S.-H. Li, Z.-R. Tang, Y.-J. Xu, Chem. Sci. 9 (2018) 8914–8922.
[12] S.K. Dutta, S.K. Mehetor, N. Pradhan, J. Phys. Chem. Lett. 6 (2015) 936–944.
[13] Y. Qu, X. Duan, Chem. Soc. Rev. 42 (2013) 2568–2580.
[14] X. Lang, X. Chen, J. Zhao, Chem. Soc. Rev. 43 (2014) 473–486.
[15] N. Zhang, C. Han, X. Fu, Y.-J. Xu, Chem 4 (2018) 1832–1861.
[16] S. Bai, J. Jiang, Q. Zhang, Y. Xiong, Chem. Soc. Rev. 44 (2015) 2893–2939.
[17] X. Liu, J. Iocozzia, Y. Wang, X. Cui, Y. Chen, S. Zhao, Z. Li, Z. Lin, Energy Environ. Sci. 10 (2017) 402–434.
[18] Y. Zhang, S. He, W. Guo, Y. Hu, J. Huang, J.R. Mulcahy, W.D. Wei, Chem. Rev. 118 (2018) 2927–2954.
[19] S.C. Warren, E. Thimsen, Energy Environ. Sci. 5 (2012) 5133–5146.
[20] S. Linic, U. Aslam, C. Boerigter, M. Morabito, Nature Mater. 14 (2015) 567–576.
[21] M.L. Brongersma, N.J. Halas, P. Nordlander, Nature Nanotechnol. 10 (2015) 25–34.
[22] J. Guo, Y. Zhang, L. Shi, Y. Zhu, M.F. Mideksa, K. Hou, W. Zhao, D. Wang, M. Zhao, X. Zhang, J. Lv, J. Zhang, X. Wang, Z. Tang, J. Am. Chem. Soc. 139 (2017) 17964–17972.
[23] H. Chen, L. Shao, Q. Li, J. Wang, Chem. Soc. Rev. 42 (2013) 2679–2724.
[24] X. Huang, S. Neretina, M.A. El-Sayed, Adv. Mater. 21 (2009) 4880–4910.
[25] A. Gole, C.J. Murphy, Chem. Mater. 16 (2004) 3633–3640.
[26] X. Ye, Y. Gao, J. Chen, D.C. Reifsnyder, C. Zheng, C.B. Murray, Nano Lett. 13 (2013) 2163–2171.
[27] X. Ye, C. Zheng, J. Chen, Y. Gao, C.B. Murray, Nano Lett. 13 (2013) 765–771.
[28] S. Liu, Z.-R. Tang, Y. Sun, J.C. Colmenares, Y.-J. Xu, Chem. Soc. Rev. 44 (2015) 5053–5075.
[29] K. Liu, N. Zhao, E. Kumacheva, Chem. Soc. Rev. 40 (2011) 656–671.
[30] J. Cao, T. Sun, K.T.V. Grattan, Sens. Actuators, B 195 (2014) 332–351.
[31] L. Vigderman, B.P. Khanal, E.R. Zubarev, Adv. Mater. 24 (2012) 4811–4841.
[32] M.J. Walsh, W. Tong, H. Katz-Boon, P. Mulvaney, J. Etheridge, A.M. Funston, Acc. Chem. Res. 50 (2017) 2925–2935.
[33] M. Meng, Z. Fang, C. Zhang, H. Su, R. He, R. Zhang, H. Li, Z.-Y. Li, X. Wu, C. Ma, J. Zeng, Nano Lett. 16 (2016) 3036–3041.
[34] O. Oviedo, E. Leiva, M. Mariscal, Phys. Chem. Chem. Phys. 10 (2008) 3561–3568.
[35] E. Carbó-Argibay, B. Rodríguez-González, S. Gómez-Graña, A. Guerrero-Martínez, I. Pastoriza-Santos, J. Pérez-Juste, L.M. Liz-Marzán, Angew. Chem. Int. Ed. 49 (2010) 9397–9400.
[36] Z.-Y. Zhou, N. Tian, J.-T. Li, I. Broadwell, S.-G. Sun, Chem. Soc. Rev. 40 (2011) 4167–4185.
[37] S. Jayabal, A. Pandikumar, H.N. Lim, R. Ramaraj, T. Sun, N.M. Huang, Analyst 140 (2015) 2540–2555.
[38] R. Jiang, B. Li, C. Fang, J. Wang, Adv. Mater. 26 (2014) 5274–5309.
[39] S. Link, M.B. Mohamed, M.A. El-Sayed, J. Phys. Chem. B 103 (1999) 3073–3077.
[40] B. Yan, Y. Wang, J. Phys. Chem. B 107 (2003) 9159–9160.
[41] N.R. Jana, L. Gearheart, C.J. Murphy, Langmuir 17 (2001) 6782–6786.
[42] P.K. Jain, K.S. Lee, I.H. El-Sayed, M.A. El-Sayed, J. Phys. Chem. B 110 (2006) 7238–7248.
[43] P.B. Johnson, R.W. Christy, Phys. Rev. B 6 (1972) 4370–4379.
[44] M. Zhang, C. Li, C. Wang, C. Zhang, Z. Wang, Q. Han, H. Zheng, Appl. Opt. 56 (2017) 375–379.
[45] K.-Q. Lin, J. Yi, S. Hu, B.-J. Liu, J.-Y. Liu, X. Wang, B. Ren, J. Phys. Chem. C 120 (2016) 20806–20813.
[46] P.G. Etchegoin, E.C. Le Ru, Phys. Chem. Chem. Phys. 10 (2008) 6079–6089.
[47] S. Linic, P. Christopher, D.B. Ingram, Nature Mater. 10 (2011) 911–921.
[48] J. Zuloaga, E. Prodan, P. Nordlander, ACS Nano 4 (2010) 5269–5276.
[49] F.C.P. Masim, H.-L. Liu, M. Porta, T. Yonezawa, A. Balčytis, S. Juodkazis, W.-H. Hsu, K. Hatanaka, Opt. Express 24 (2016) 14781–14792.
[50] T. Ming, L. Zhao, Z. Yang, H. Chen, L. Sun, J. Wang, C. Yan, Nano Lett. 9 (2009) 3896–3903.
[51] M. Grzelczak, J. Pérez-Juste, F.J. García de Abajo, L.M. Liz-Marzán, J. Phys. Chem. C 111 (2007) 6183–6188.
[52] W.R. Erwin, H.F. Zarick, E.M. Talbert, R. Bardhan, Energy Environ. Sci. 9 (2016) 1577–1601.
[53] M. Xiao, R. Jiang, F. Wang, C. Fang, J. Wang, J.C. Yu, J. Mater. Chem. A 1 (2013) 5790–5805.
[54] M. Wang, M. Ye, J. Iocozzia, C. Lin, Z. Lin,Adv. Sci. 3 (2016), 1600024.
[55] S.K. Cushing, J. Li, F. Meng, T.R. Senty, S. Suri, M. Zhi, M. Li, A.D. Bristow, N. Wu, J. Am. Chem. Soc. 134 (2012) 15033–15041.
[56] M. Gao, P.K.N. Connor, G.W. Ho, Energy Environ. Sci. 9 (2016) 3151–3160.
[57] X. Li, X. Zhang, H.O. Everitt, J. Liu, Nano Lett, Nano Lett. (2019), http://dx.doi.org/10.1021/acs.nanolett.1028b04706.
[58] Y. Li, J. Jin, D. Wang, J. Lv, K. Hou, Y. Liu, C. Chen, Z. Tang, Nano Res. 11 (2018) 3294–3305.
[59] H. Huang, L. Zhang, Z. Lv, R. Long, C. Zhang, Y. Lin, K. Wei, C. Wang, L. Chen, Z.-Y. Li, Q. Zhang, Y. Luo, Y. Xiong, J. Am. Chem. Soc. 138 (2016) 6822–6828.
[60] G. Baffou, R. Quidant, C. Girard,Appl. Phys. Lett. 94 (2009), 153109.
[61] C. Li, P. Wang, Y. Tian, X. Xu, H. Hou, M. Wang, G. Qi, Y. Jin, ACS Catal. 7 (2017) 5391–5398.
[62] H. Wang, T. You, W. Shi, J. Li, L. Guo, J. Phys. Chem. C 116 (2012) 6490–6494.
[63] X. Wu, X. Shi, Y. Ji, S. Hou, W. Liu, H. Zhang, T. Wen, J. Yan, M. Song, Z. Hu, Langmuir 31 (2015) 1537–1546.
[64] J.-J. Chen, J.C.S. Wu, P.C. Wu, D.P. Tsai, J. Phys. Chem. C 116 (2012) 26535–26542.
[65] W. Hou, S.B. Cronin, Adv. Funct. Mater. 23 (2013) 1612–1619.
[66] X. Wang, M. Zhu, Y. Sun, W. Fu, Q. Gu, C. Zhang, Y. Zhang, Y. Dai, Y. Sun, Part. Part. Syst. Charact. 33 (2016) 140–149.
[67] W.R. Erwin, A. Coppola, H.F. Zarick, P. Arora, K.J. Miller, R. Bardhan, Nanoscale 6 (2014) 12626–12634.
[68] B. Li, T. Gu, T. Ming, J. Wang, P. Wang, J. Wang, J.C. Yu, ACS Nano 8 (2014) 8152–8162.
[69] Z. Zheng, T. Tachikawa, T. Majima, Chem. Commun. 51 (2015) 14373–14376.
[70] X. Wang, C. Liow, A. Bisht, X. Liu, T.C. Sum, X. Chen, S. Li, Adv. Mater. 27 (2015) 2207–2214.
[71] A. Tanaka, K. Nakanishi, R. Hamada, K. Hashimoto, H. Kominami, ACS Catal. 3 (2013) 1886–1891.
[72] L. Kong, W. Chen, D. Ma, Y. Yang, S. Liu, S. Huang, J. Mater. Chem. 22 (2012) 719–724.
[73] J. Wu, Z. Zhang, B. Liu, Y. Fang, L. Wang, B. Dong,Solar RRL 2 (2018), 1800039.
[74] Y. Shi, J. Wang, C. Wang, T.-T. Zhai, W.-J. Bao, J.-J. Xu, X.-H. Xia, H.-Y. Chen, J. Am. Chem. Soc. 137 (2015) 7365–7370.
[75] Y. Si, S. Cao, Z. Wu, Y. Ji, Y. Mi, X. Wu, X. Liu, L. Piao, Appl. Catal. B: Environ. 220 (2018) 471–476.
[76] J.W. Ha, T.P.A. Ruberu, R. Han, B. Dong, J. Vela, N. Fang, J. Am. Chem. Soc. 136 (2014) 1398–1408.
[77] Z. Yin, B. Chen, M. Bosman, X. Cao, J. Chen, B. Zheng, H. Zhang, Small 10 (2014) 3537–3543.
[78] M.S. Arshad, Š. Trafela, K.Ž. Rožman, J. Kovač, P. Djinović, A. Pintar, J. Mater. Chem. C 5 (2017) 10509–10516.
[79] X. Cai, L. Mao, S. Yang, K. Han, J. Zhang, ACS Energy Lett. 3 (2018) 932–939.
[80] J. Pérez-Juste, I. Pastoriza-Santos, L.M. Liz-Marzán, P. Mulvaney, Coord. Chem. Rev. 249 (2005) 1870–1901.
[81] S.E. Lohse, C.J. Murphy, Chem. Mater. 25 (2013) 1250–1261.
[82] X. Wang, M. Shao, S. Zhang, X. Liu, J. Nanopart. Res. 15 (2013) 1892.
[83] M. Grzelczak, J. Pérez-Juste, P. Mulvaney, L.M. Liz-Marzán, Chem. Soc. Rev. 37 (2008) 1783–1791.
[84] Y.-Y. Yu, S.-S. Chang, C.-L. Lee, C.R.C. Wang, J. Phys. Chem. B 101 (1997) 6661–6664.
[85] F. Kim, J.H. Song, P. Yang, J. Am. Chem. Soc. 124 (2002) 14316–14317.
[86] S. Neretina, W. Qian, E. Dreaden, M.A. El-Sayed, R.A. Hughes, J.S. Preston, P. Mascher, Nano Lett. 8 (2008) 2410–2418.
[87] V.M. Cepak, C.R. Martin, J. Phys. Chem. B 102 (1998) 9985–9990.
[88] B. Nikoobakht, M.A. El-Sayed, Chem. Mater. 15 (2003) 1957–1962.
[89] H. Wang, Z. Sun, Q. Lu, F. Zeng, D. Su, Small 8 (2012) 1167–1172.
[90] S. Liang, J.-B. Li, M. Li, X. Tang, Plasmonics 13 (2018) 181–187.
[91] Z.W. Seh, S. Liu, S.-Y. Zhang, M.S. Bharathi, H. Ramanarayan, M. Low, K.W. Shah, Y.-W. Zhang, M.-Y. Han, Angew. Chem. Int. Ed. 50 (2011) 10140–10143.
[92] B. Wu, D. Liu, S. Mubeen, T.T. Chuong, M. Moskovits, G.D. Stucky, J. Am. Chem. Soc. 138 (2016) 1114–1117.
[93] N. Zhou, H. Zhu, S. Li, J. Yang, T. Zhao, Y. Li, Q.-H. Xu, J. Phys. Chem. C 122 (2018) 7824–7830.
[94] Y. Yang, S. Han, G. Zhou, L. Zhang, X. Li, C. Zou, S. Huang, Nanoscale 5 (2013) 11808–11819.
[95] H. Sun, J. He, J. Wang, S.-Y. Zhang, C. Liu, T. Sritharan, S. Mhaisalkar, M.-Y. Han, D. Wang, H. Chen, J. Am. Chem. Soc. 135 (2013) 9099–9110.
[96] M. Li, X.-F. Yu, S. Liang, X.-N. Peng, Z.-J. Yang, Y.-L. Wang, Q.-Q. Wang, Adv. Funct. Mater. 21 (2011) 1788–1794.
[97] Y.-T. Zhou, W. He, W.G. Wamer, X. Hu, X. Wu, Y.M. Lo, J.-J. Yin, Nanoscale 5 (2013) 1583–1591.
[98] G. Su, H. Jiang, H. Zhu, J.-J. Lv, G. Yang, B. Yan, J.-J. Zhu, Nanoscale 9 (2017) 12494–12502.
[99] S. Hou, X. Hu, T. Wen, W. Liu, X. Wu, Adv. Mater. 25 (2013) 3857–3862.
[100] A. Li, W. Zhu, C. Li, T. Wang, J. Gong, Chem. Soc. Rev. (2019).
[101] K. Park, L.F. Drummy, R.A. Vaia, J. Mater. Chem. 21 (2011) 15608–15618.
[102] J. Huang, Y. Zhu, C. Liu, Y. Zhao, Z. Liu, M.N. Hedhili, A. Fratalocchi, Y. Han, Small 11 (2015) 5214–5221.
[103] N.S. Abadeer, M.R. Brennan, W.L. Wilson, C.J. Murphy, ACS Nano 8 (2014) 8392–8406.
[104] W. Shang, C. Zeng, Y. Du, H. Hui, X. Liang, C. Chi, K. Wang, Z. Wang, J. Tian,Adv. Mater. 29 (2017), 1604381.
[105] Y. Su, H. Xu, J. Wang, X. Luo, Z.-I. Xu, K. Wang, W. Wang, Nano Res. 12 (2019) 625–630.
[106] J. Li, H.C. Zeng, Angew. Chem. Int. Ed. 44 (2005) 4342–4345.
[107] Y. Si, S. Cao, Z. Wu, Y. Ji, Y. Mi, X. Wu, X. Liu, L. Piao, Nano Energy 41 (2017) 488–493.
[108] Q. Ruan, C. Fang, R. Jiang, H. Jia, Y. Lai, J. Wang, H.-Q. Lin, Nanoscale 8 (2016) 6514–6526.
[109] S.-U. Lee, H. Jung, D.H. Wi, J.W. Hong, J. Sung, S.-I. Choi, S.W. Han, J. Mater. Chem. A 6 (2018) 4068–4078.
[110] M. Ji, M. Xu, W. Zhang, Z. Yang, L. Huang, J. Liu, Y. Zhang, L. Gu, Y. Yu, W. Hao, P. An, L. Zheng, H. Zhu, J. Zhang, Adv. Mater. 28 (2016) 3094–3101.

[111] D. Seo, G. Park, H. Song, J. Am. Chem. Soc. 134 (2012) 1221–1227.
[112] A. Li, P. Zhang, X. Chang, W. Cai, T. Wang, J. Gong, Small 11 (2015) 1892–1899.
[113] X. Li, T. Zhao, Y. Lu, P. Wang, A.M. El-Toni, F. Zhang, D. Zhao,Adv. Mater. 29 (2017), 1701652.
[114] L. Zhang, T. Wang, L. Yang, C. Liu, C. Wang, H. Liu, Y.A. Wang, Z. Su, Chem. Eur. J. 18 (2012) 12512–12521.
[115] J. Liu, S.Z. Qiao, J.S. Chen, X.W. Lou, X. Xing, G.Q. Lu, Chem. Commun. 47 (2011) 12578–12591.
[116] N. Meir, I. Jen-La Plante, K. Flomin, E. Chockler, B. Moshofsky, M. Diab, M. Volokh, T. Mokari, J. Mater. Chem. A 1 (2013) 1763–1769.
[117] X. Yu, J. Bi, G. Yang, H. Tao, S. Yang, J. Phys. Chem. C 120 (2016) 24533–24541.
[118] N. Li, J. Wu, H.-B. Fang, X.-H. Zhang, Y.-Z. Zheng, X. Tao, Appl. Surf. Sci. 448 (2018) 41–49.
[119] J. Wu, Y. Liu, Y. Tang, S. Wang, C. Wang, Y. Li, X. Su, J. Tian, Y. Tian, J. Pan, Y. Su, H. Zhu, Z. Teng, G. Lu, ACS Appl. Mater. Interfaces 8 (2016) 17927–17935.
[120] Y. Liu, W. Zhang, S. Li, C. Cui, J. Wu, H. Chen, F. Huo, Chem. Mater. 26 (2014) 1119–1125.
[121] E.C. Cho, P.H. Camargo, Y. Xia, Adv. Mater. 22 (2010) 744–748.
[122] M. Lin, Y. Wang, X. Sun, W. Wang, L. Chen, ACS Appl. Mater. Interfaces 7 (2015) 7516–7525.
[123] M. Lattuada, T.A. Hatton, Nano Today 6 (2011) 286–308.
[124] J. Du, R.K. O'Reilly, Chem. Soc. Rev. 40 (2011) 2402–2416.
[125] D. Wang, Z. Li, J. Zhou, H. Fang, X. He, P. Jena, J.-B. Zeng, W.-N. Wang, Nano-Micro Lett. 10 (2017) 4.
[126] C. Yu, W. Zhou, L. Zhu, G. Li, K. Yang, R. Jin, Appl. Catal. B: Environ. 184 (2016) 1–11.
[127] Y. Lu, J. Yuan, F. Polzer, M. Drechsler, J. Preussner, ACS Nano 4 (2010) 7078–7086.
[128] P.-G. de Gennes, Angew. Chem. Int. Ed. Engl. 31 (1992) 842–845.
[129] Z. Wang, B. He, G. Xu, G. Wang, J. Wang, Y. Feng, D. Su, B. Chen, H. Li, Z. Wu, H. Zhang, L. Shao, H. Chen, Nature Commun. 9 (2018) 563.
[130] J. Huang, Y. Zhu, M. Lin, Q. Wang, L. Zhao, Y. Yang, K.X. Yao, Y. Han, J. Am. Chem. Soc. 135 (2013) 8552–8561.
[131] X. Guo, Q. Zhang, Y. Sun, Q. Zhao, J. Yang, ACS Nano 6 (2012) 1165–1175.
[132] D. Seo, C.I. Yoo, J. Jung, H. Song, J. Am. Chem. Soc. 130 (2008) 2940–2941.
[133] C. Li, L. Sun, Y. Sun, T. Teranishi, Chem. Mater. 25 (2013) 2580–2590.
[134] S. Chen, S.V. Jenkins, J. Tao, Y. Zhu, J. Chen, J. Phys. Chem. C 117 (2013) 8924–8932.
[135] Z. Zheng, T. Tachikawa, T. Majima, J. Am. Chem. Soc. 136 (2014) 6870–6873.
[136] S. Liang, X.-L. Liu, Y.-Z. Yang, Y.-L. Wang, J.-H. Wang, Z.-J. Yang, L.-B. Wang, S.-F. Jia, X.-F. Yu, L. Zhou, J.-B. Wang, J. Zeng, Q.-Q. Wang, Z. Zhang, Nano Lett. 12 (2012) 5281–5286.
[137] F. Wang, C. Li, H. Chen, R. Jiang, L.-D. Sun, Q. Li, J. Wang, J.C. Yu, C.-H. Yan, J. Am. Chem. Soc. 135 (2013) 5588–5601.
[138] C. Han, Q. Quan, H.M. Chen, Y. Sun, Y.-J. Xu,Small 13 (2017), 1602947.
[139] L. Liu, S. Ouyang, J. Ye, Angew. Chem. Int. Ed. 52 (2013) 6689–6693.
[140] C. Han, N. Zhang, Y.-J. Xu, Nano Today 11 (2016) 351–372.
[141] X. Cai, M. Zhu, O.A. Elbanna, M. Fujitsuka, S. Kim, L. Mao, J. Zhang, T. Majima, ACS Catal. 8 (2018) 122–131.
[142] N. Zhang, C. Han, Y.-J. Xu, J.J. Foley IV, D. Zhang, J. Codrington, S.K. Gray, Y. Sun, Nature Photon. 10 (2016) 473–482.
[143] L. Xu, C. Hao, H. Yin, L. Liu, W. Ma, L. Wang, H. Kuang, C. Xu, J. Phys. Chem. Lett. 4 (2013) 2379–2384.
[144] H. Chen, F. Wang, K. Li, K.C. Woo, J. Wang, Q. Li, L.-D. Sun, X. Zhang, H.-Q. Lin, C.-H. Yan, ACS Nano 6 (2012) 7162–7171.
[145] Y. Qu, R. Cheng, Q. Su, X. Duan, J. Am. Chem. Soc. 133 (2011) 16730–16733.
[146] C. Hu, J. Rong, J. Cui, Y. Yang, L. Yang, Y. Wang, Y. Liu, Carbon 51 (2013) 255–264.
[147] P. Zhang, M. Fujitsuka, T. Majima, Nanoscale 9 (2017) 1520–1526.
[148] Y. Kang, Y. Gong, Z. Hu, Z. Li, Z. Qiu, X. Zhu, P.M. Ajayan, Z. Fang, Nanoscale 7 (2015) 4482–4488.
[149] Y.-C. Pu, G. Wang, K.-D. Chang, Y. Ling, Y.-K. Lin, B.C. Fitzmorris, C.-M. Liu, X. Lu, Y. Tong, J.Z. Zhang, Nano Lett. 13 (2013) 3817–3823.
[150] H. Sun, S. Zeng, Q. He, P. She, K. Xu, Z. Liu, Dalton Trans. 46 (2017) 3887–3894.
[151] P. Kannan, F. Abdul Rahim, R. Chen, X. Teng, L. Huang, H. Sun, D.-H. Kim, ACS Appl. Mater. Interfaces 5 (2013) 3508–3513.
[152] P. She, K. Xu, Y. Shang, Q. He, S. Zeng, S. Yin, G. Lu, S. Liang, H. Sun, Z. Liu, New J. Chem. 42 (2018) 3315–3321.
[153] I. Pastoriza-Santos, D. Gomez, J. Pérez-Juste, L.M. Liz-Marzán, P. Mulvaney, Phys. Chem. Chem. Phys. 6 (2004) 5056–5060.
[154] J.H. Song, F. Kim, D. Kim, P. Yang, Chem. Eur. J. 11 (2005) 910–916.
[155] X. Chen, S. Shen, L. Guo, S.S. Mao, Chem. Rev. 110 (2010) 6503–6570.
[156] X. Meng, T. Wang, L. Liu, S. Ouyang, P. Li, H. Hu, T. Kako, H. Iwai, A. Tanaka, J. Ye, Angew. Chem. Int. Ed. 53 (2014) 11478–11482.
[157] R. Singh, B. Pal, J. Mol. Catal. A Chem. 378 (2013) 246–254.
[158] K.K. Patra, C.S. Gopinath, J. Phys. Chem. C 122 (2018) 1206–1214.
[159] X. Yu, F. Liu, J. Bi, B. Wang, S. Yang, Nano Energy 33 (2017) 469–475.
[160] J. Zhang, F. Zhao, Z. Zhang, N. Chen, L. Qu, Nanoscale 5 (2013) 3112–3126.
[161] X. Chen, L. Liu, F. Huang, Chem. Soc. Rev. 44 (2015) 1861–1885.
[162] X. Wang, R. Long, D. Liu, D. Yang, C. Wang, Y. Xiong, Nano Energy 24 (2016) 87–93.
[163] C. Xu, W. Huang, Z. Li, B. Deng, Y. Zhang, M. Ni, K. Cen, ACS Catal. 8 (2018) 6582–6593.
[164] B. Sun, W. Zhou, H. Li, L. Ren, P. Qiao, W. Li, H. Fu,Adv. Mater. 30 (2018), 1804282.
[165] C. Fang, H. Jia, S. Chang, Q. Ruan, P. Wang, T. Chen, J. Wang, Energy Environ. Sci. 7 (2014) 3431–3438.
[166] M.C. Ortega-Liebana, J.L. Hueso, R. Arenal, J. Santamaria, Nanoscale 9 (2017) 1787–1792.
[167] C. Han, M.-Q. Yang, N. Zhang, Y.-J. Xu, J. Mater. Chem. A 2 (2014) 19156–19166.
[168] P. Roy, A.P. Periasamy, C.-T. Liang, H.-T. Chang, Environ. Sci. Technol. 47 (2013) 6688–6695.
[169] J.B. Lee, S. Choi, J. Kim, Y.S. Nam, Nano Today 16 (2017) 61–81.
[170] C. Li, T. Wang, Z.-J. Zhao, W. Yang, J.-F. Li, A. Li, Z. Yang, G.A. Ozin, J. Gong, Angew. Chem. Int. Ed. 57 (2018) 5278–5282.
[171] T.G.U. Ghobadi, A. Ghobadi, E. Ozbay, F. Karadas, ChemPhotoChem 2 (2018) 161–182.
[172] A. Fujishima, K. Honda, Nature 238 (1972) 37–38.
[173] A. Mao, G.Y. Han, J.H. Park, J. Mater. Chem. 20 (2010) 2247–2250.
[174] Y. Nishijima, K. Ueno, Y. Kotake, K. Murakoshi, H. Inoue, H. Misawa, J. Phys. Chem. Lett. 3 (2012) 1248–1252.
[175] K.H.W. Ho, A. Shang, F. Shi, T.W. Lo, P.H. Yeung, Y.S. Yu, X. Zhang, K.-y. Wong, D.Y. Lei,Adv. Funct. Mater. 28 (2018), 1800383.
[176] S. Mubeen, J. Lee, D. Liu, G.D. Stucky, M. Moskovits, Nano Lett. 15 (2015) 2132–2136.
[177] J. Lee, S. Mubeen, X. Ji, G.D. Stucky, M. Moskovits, Nano Lett. 12 (2012) 5014–5019.
[178] Z. Li, W. Wang, S. Liao, M. Liu, Y. Qi, C. Ding, C. Li, Energy Environ. Sci. (2019), http://dx.doi.org/10.1039/C1038EE01299G.
[179] J. Li, N. Wu, Catal. Sci. Technol. 5 (2015) 1360–1384.
[180] B. You, X. Liu, N. Jiang, Y. Sun, J. Am. Chem. Soc. 138 (2016) 13639–13646.
[181] S. Sarina, E.R. Waclawik, H. Zhu, Green Chem. 15 (2013) 1814–1833.
[182] Z. Zheng, T. Tachikawa, T. Majima, J. Am. Chem. Soc. 137 (2014) 948–957.
[183] R. Long, Z. Rao, K. Mao, Y. Li, C. Zhang, Q. Liu, C. Wang, Z.-Y. Li, X. Wu, Y. Xiong, Angew. Chem. Int. Ed. 127 (2015) 2455–2460.
[184] J.D. Xiao, L. Han, J. Luo, S.H. Yu, H.L. Jiang, Angew. Chem. Int. Ed. 57 (2018) 1103–1107.
[185] Y. Li, G. Pan, Q. Liu, L. Ma, Y. Xie, L. Zhou, Z. Hao, Q. Wang, ChemPhysChem 19 (2018) 1852–1858.
[186] R. Long, K. Mao, M. Gong, S. Zhou, J. Hu, M. Zhi, Y. You, S. Bai, J. Jiang, Q. Zhang, Angew. Chem. Int. Ed. 126 (2014) 3269–3273.
[187] A. Tanaka, K. Hashimoto, H. Kominami, J. Am. Chem. Soc. 136 (2014) 586–589.
[188] X. Zhang, X. Li, D. Zhang, N.Q. Su, W. Yang, H.O. Everitt, J. Liu, Nature Commun. 8 (2017) 14542.
[189] S. Wang, P. Chen, Y. Bai, J.-H. Yun, G. Liu, L. Wang,Adv. Mater. 30 (2018), 1800486.
[190] S. Kundu, A. Patra, Chem. Rev. 117 (2017) 712–757.
[191] W. Jiang, S. Bai, L. Wang, X. Wang, L. Yang, Y. Li, D. Liu, X. Wang, Z. Li, J. Jiang, Y. Xiong, Small 12 (2016) 1640–1648.
[192] X. Xia, N. Deng, G. Cui, J. Xie, X. Shi, Y. Zhao, Q. Wang, W. Wang, B. Tang, Chem. Commun. 51 (2015) 10899–10902.
[193] O. Elbanna, S. Kim, M. Fujitsuka, T. Majima, Nano Energy 35 (2017) 1–8.
[194] L. Ma, S. Liang, X.-L. Liu, D.-J. Yang, L. Zhou, Q.-Q. Wang, Adv. Funct. Mater. 25 (2015) 898–904.
[195] Q. Li, B. Guo, J. Yu, J. Ran, B. Zhang, H. Yan, J.R. Gong, J. Am. Chem. Soc. 133 (2011) 10878–10884.
[196] D. Ding, K. Liu, S. He, C. Gao, Y. Yin, Nano Lett. 14 (2014) 6731–6736.
[197] S.M. Majhi, P. Rai, S. Raj, B.-S. Chon, K.-K. Park, Y.-T. Yu, ACS Appl. Mater. Interfaces 6 (2014) 7491–7497.
[198] X. Wang, C. Liow, D. Qi, B. Zhu, W.R. Leow, H. Wang, C. Xue, X. Chen, S. Li, Adv. Mater. 26 (2014) 3506–3512.
[199] Y.-Y. Li, J.-H. Wang, Z.-J. Luo, K. Chen, Z.-Q. Cheng, L. Ma, S.-J. Ding, L. Zhou, Q.-Q. Wang, Sci. Rep. 7 (2017) 7178.
[200] L. Yuan, B. Weng, J.C. Colmenares, Y. Sun, Y.-J. Xu,Small 13 (2017), 1702253.
[201] J. Zhu, Y. Yang, L. Chen, W. Xiao, H. Liu, H.D. Abruña, D. Wang, Chem. Mater. 30 (2018) 5987–5995.
[202] X.-J. Wu, J. Chen, C. Tan, Y. Zhu, Y. Han, H. Zhang, Nature Chem. 8 (2016) 470.
[203] A. Li, X. Chang, Z. Huang, C. Li, Y. Wei, L. Zhang, T. Wang, J. Gong, Angew. Chem. Int. Ed. 55 (2016) 13734–13738.
[204] K. Chang, Z. Mei, T. Wang, Q. Kang, S. Ouyang, J. Ye, ACS Nano 8 (2014) 7078–7087.
[205] S. Mubeen, J. Lee, N. Singh, S. Krämer, G.D. Stucky, M. Moskovits, Nature Nanotech. 8 (2013) 247.
[206] P. Yang, J.-M. Tarascon, Nature Mater. 11 (2012) 560.
[207] C. Clavero, Nature Photon. 8 (2014) 95–103.
[208] S. Bai, X. Li, Q. Kong, R. Long, C. Wang, J. Jiang, Y. Xiong, Adv. Mater. 27 (2015) 3444–3452.
[209] H. Liu, C. Xu, D. Li, H.L. Jiang, Angew. Chem. Int. Ed. 130 (2018) 5477–5481.
[210] S. Meng, X. Ye, J. Zhang, X. Fu, S. Chen, J. Catal. 367 (2018) 159–170.
[211] J. Yang, Y. Guo, W. Lu, R. Jiang, J. Wang,Adv. Mater. 30 (2018), 1802227.
[212] C. Han, Z.-R. Tang, J. Liu, S. Jin, Y.-J. Xu, Chem. Sci. 10 (2019) 3514–3522.
[213] L. Zhou, D.F. Swearer, C. Zhang, H. Robatjazi, H. Zhao, L. Henderson, L. Dong, P. Christopher, E.A. Carter, P. Nordlander, N.J. Halas, Science 362 (2018) 69–72.
[214] E. Cortés, Science 362 (2018) 28–29.
[215] X. Ke, S. Sarina, J. Zhao, X. Zhang, J. Chang, H. Zhu, Chem. Commun. 48 (2012) 3509–3511.

[216] S. Sarina, H.-Y. Zhu, Q. Xiao, E. Jaatinen, J. Jia, Y. Huang, Z. Zheng, H. Wu, Angew. Chem. Int. Ed. 53 (2014) 2935–2940.
[217] M.J. Kale, T. Avanesian, P. Christopher, ACS Catal. 4 (2014) 116–128.
[218] N. Zou, G. Chen, X. Mao, H. Shen, E. Choudhary, X. Zhou, P. Chen, ACS Nano 12 (2018) 5570–5579.
[219] S. Mubeen, J. Lee, N. Singh, S. Krämer, G.D. Stucky, M. Moskovits, Nature Nanotechnol. 8 (2013) 247–251.
[220] H. Wang, Y. Gao, J. Liu, X. Li, M. Ji, E. Zhang, X. Cheng, M. Xu, J. Liu, H. Rong, W. Chen, F. Fan, C. Li, J. Zhang, Adv. Energy Mater. 1803889.
[221] C. Leng, X. Zhang, F. Xu, Y. Yuan, H. Pei, Z. Sun, L. Li, Z. Bao,Small 14 (2018), 1703077.
[222] S. Zeng, H. Sun, Y. Wu, Y. Shang, P. She, Q. He, S. Yin, Z. Liu, Inorg. Chem. Front. 5 (2018) 626–634.
[223] Z. Liu, Y. Liu, P. Xu, Z. Ma, J. Wang, H. Yuan, ACS Appl. Mater. Interfaces 9 (2017) 20620–20629.
[224] Y. Li, J. Zhao, W. You, D. Cheng, W. Ni, Nanoscale 9 (2017) 3925–3933.
[225] D. Kumar, A. Lee, T. Lee, M. Lim, D.-K. Lim, Nano Lett. 16 (2016) 1760–1767.

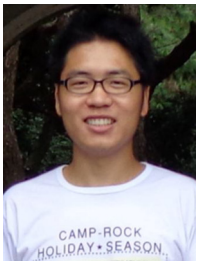

Chuang Han is now pursing his Ph.D. degree with the supervision of Prof. Yi-Jun Xu at State Key Laboratory of Photocatalysis on Energy and Environment, College of Chemistry, Fuzhou University, P. R. China. His main research interests include the plasmon-enhanced and carbon-enhanced heterogeneous photocatalysis.

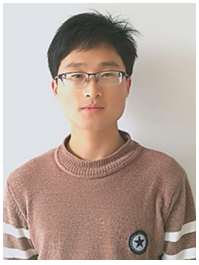

Ming-Yu Qi is now pursuing his Ph.D. degree under the supervision of Prof. Yi-Jun Xu at State Key Laboratory of Photocatalysis on Energy and Environment, College of Chemistry, Fuzhou University, P. R. China. His current research interests include the fabrication of composites for functional applications in heterogeneous photocatalysis.

Zi-Rong Tang is an associate professor now working at the College of Chemistry, Fuzhou University, P. R. China. Her current research interests primarily focus on the fabrication of one dimensional semiconductor-based and carbon-based composite materials and their multifunctional applications in heterogeneous photocatalysis and thermocatalysis.

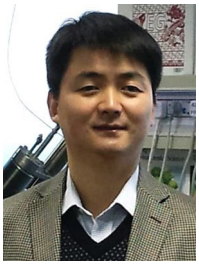

Jinlong Gong is a faculty of chemical engineering at Tianjin University, P. R. China, where he currently holds a Cheung Kong Chair Professorship. He is a Fellow of Royal Society of Chemistry (FRSC) and his research interests include catalytic conversions of green energy, utilization of carbon oxides, and synthesis and applications of nanostructured materials.

Yi-Jun Xu is a full professor working at the State Key Laboratory of Photocatalysis on Energy and Environment, College of Chemistry, Fuzhou University, P. R. China. He is a Fellow of Royal Society of Chemistry (FRSC) and his research interest focuses on the synthesis and applications of composite materials, such as graphene-based composites, core-shell structured composites and metal-based nanostructured hybrid materials, in the field of heterogeneous photocatalysis.